1

Zircon as Magma Monitor: Robust, Temperature-Dependent Partition Coefficients from Glass and Zircon Surface and Rim Measurements from Natural Systems

Lily L. Claiborne[1], Calvin F. Miller[1], Guillherme A. R. Gualda[1], Tamara L. Carley[2], Aaron K. Covey[1], Joseph L. Wooden[3], and Marc A. Fleming[1]

ABSTRACT

Analysis of natural mineral/host glass pairs provides robust zircon-melt partition coefficients applicable to natural systems. We analyzed zircon rims (outer ~15 μm of grain interiors) or surfaces (1–2 μm deep pits on crystal faces) and glasses in tholeiitic, calc-alkaline, and alkaline dacites and rhyolites from diverse settings (continental extension, AZ-NV, USA; hot spot/spreading center, Iceland; continental arc, Mount St. Helens (MSH), WA, USA). MSH Kds are based on eruption-age surfaces with adhering glass, which should closely approach crystal-melt equilibrium. We parameterize trivalent rare earth element (REE) Kds by $X^*[Ti]^y$ for Sm to Lu, Nb, Th, and U, where $X = 2.5–3600$ and $y = -0.73$ to -1.3 for Sm to Lu. Kds for all elements span more than an order of magnitude but are highly coherent. REE Kds fit lattice strain model parabolas well, and all Kds show strong negative correlations with T indicators. Useful Kds for zircon can be estimated from Ti_{zircon}-$Kd_{element}$ correlations. MSH Kds based on surface analyses are consistent with those from conventional rim analysis. When paired with zircon ages, modeled compositions of MSH melts corroborate and strengthen previous conclusions regarding history and evolution of the MSH magmatic system through time.

1.1. INTRODUCTION

Zircon has become the primary tool of choice for many studies aiming to elucidate the evolution of and processes within Earth's crust [e.g., *Valley et al.*, 2005; *Watson and Harrison*, 2005; *Kemp et al.*, 2007; *Harrison*, 2009; *Condie et al.*, 2011; *Bell et al.*, 2014; *Hawkesworth et al.*, 2016]. In addition to being a reliable and durable geochronometer that can yield precise crystallization ages ranging from thousands of years to the time of the planet's formation, its isotopic and elemental compositions provide time-stamped records of its origins and conditions of growth [e.g., *Claiborne et al.*, 2006, 2010; *Kemp et al.*, 2006; *Schmitt et al.*, 2010; *Barboni et al.*, 2016]. We focus here on elemental compositions. Concentrations of elements in zircon crystals, when combined with reliable partition coefficients (Kds: concentration of element in crystal/concentration in coexisting melt) can reveal the compositions of melts from which the crystals have grown, even when no other record of their host magmas exists. This capability is most obviously relevant to detrital zircon grains, which are totally divorced from their original host materials: most dramatically represented by >4 Ga Hadean crystals, older than any known rocks, that are found in sandstones [e.g., *Froude et al.*, 1983; *Compston and Pidgeon*, 1986; *Maas et al.*, 1992; and many more over the past quarter century]. It is equally relevant to interiors of zircon crystals which, even when

[1] *Department of Earth and Environmental Sciences, Vanderbilt University, Nashville, Tennessee, USA*

[2] *Department of Geology and Environmental Geosciences, Lafayette College, Easton, Pennsylvania*

[3] *U.S. Geological Survey, Menlo Park, California, USA*

Microstructural Geochronology: Planetary Records Down to Atom Scale, Geophysical Monograph 232, First Edition.
Edited by Desmond E. Moser, Fernando Corfu, James R. Darling, Steven M. Reddy, and Kimberly Tait.

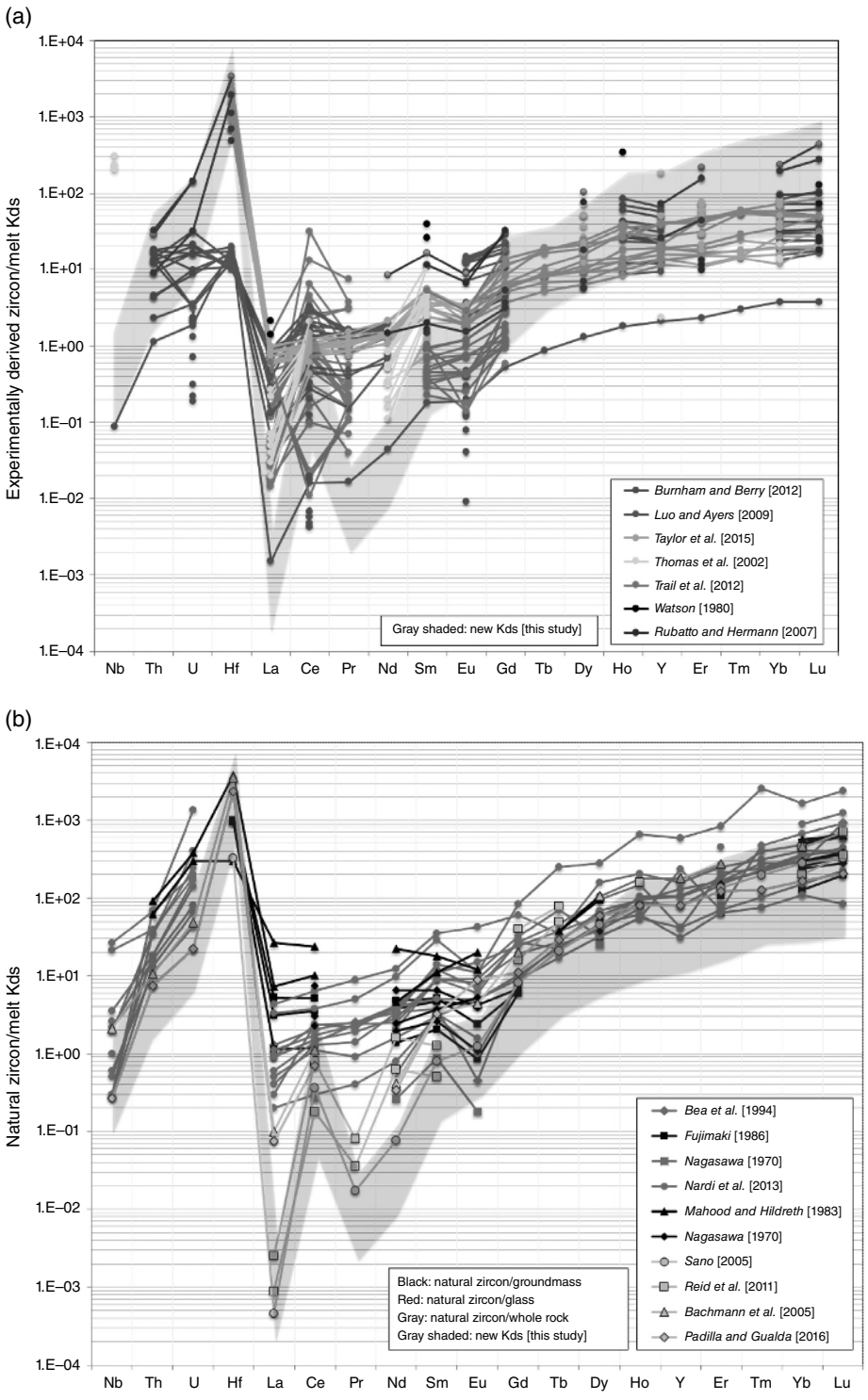

Figure 1.1 Compilation of zircon-melt Kds from the literature. The gray field represents the range of Kds calculated in this study. (a) Studies of experimental zircon [*Watson*, 1980; *Thomas et al.*, 2002; *Luo and Ayers*, 2009; *Burnham and Berry*, 2012; *Trail et al.*, 2012; *Taylor et al.*, 2015]. (b) Studies of natural zircon [*Nagasawa*, 1970; *Mahood and Hildreth*, 1983; *Fujimaki*, 1986; *Bea et al.*, 1994; *Bachmann et al.*, 2005; *Sano et al.*, 2002; *Rubatto and Hermann*, 2007; *Reid et al.*, 2011; *Nardi et al.*, 2013; *Padilla and Gualda*, 2016]. (*See insert for color representation of the figure.*)

found in recently erupted volcanic rocks, may record information about growth in magmas that were very different from those that transported them to the surface [*Claiborne et al.*, 2010].

Robust zircon Kds have, however, proven elusive: experiments are conducted with materials that do not reflect natural compositions and/or with durations that are too short for growth and equilibration of analytically tractable crystals; because zircon crystals are commonly strongly zoned and contain small inclusions, analyses do not reflect a composition that equilibrated with melt; and most Kds from natural materials are hampered by the fact that melt compositions from which zircons grew are unknown. Figure 1.1 illustrates existing zircon Kds from the literature: for individual elements, they vary by three to five orders of magnitude. Although patterns are similar (subparallel) in a very general way, in detail patterns fan and cross each other. These characteristics of the published Kd data set raise the following questions: (i) Which existing studies reflect valid Kds, and for which elements? (ii) How much of this apparent extreme variability is real? [e.g., *Hanchar and van Westrenen*, 2007] (iii) Assuming that at least some of the variability is real, what controls it? (iv) If the controls of true variability can be identified, can this lead to selection of useful values that can be applied to specific zircon compositions?

In this paper, we present partition coefficients that have been determined by analyzing zircon-glass pairs that we interpret to be cognate: that is, the analyzed zircon apparently grew from melt represented by the glass. For most of our samples, we used conventional in situ zircon rim analyses (outermost zone of cross-sectioned grains). For a subset of samples, we determined compositions of zircon surfaces (crystal faces) with adhering glass, which come as close as possible to representing zircon grown from existing host melt (glass). We compare results by surface and conventional analysis and evaluate our calculated Kds in the context of estimated temperature and melt composition, as these variables may be responsible for considerable natural variation: perhaps a substantial part of the enormous variability in published Kds. Our sample set is from three diverse tectonomagmatic settings: the Colorado River Extensional Corridor, USA (CREC; continental extension), Iceland (mid-ocean rift/hotspot), and Mount St. Helens, USA (MSH; continental subduction-related arc). We demonstrate that Kds correlate strongly with proxies for temperature of zircon growth and propose an approach for estimating Kds based upon Ti concentration within analyzed zircon zones. This approach has promise for improved constraints on the compositions of melts from which zircons grew and thereby for better understanding of Earth processes through time.

1.2. THE SAMPLE SET

Table 1.1 summarizes general characteristics of the 10 samples for which we present new data, along with three samples earlier described in *Colombini et al.* [2011].

The seven Icelandic samples were collected from six central volcanoes that span the range of tectonomagmatic settings of Iceland: active rift, propagating rift, and off-rift. All but one are from areas that are volcanically active, and three are from historical eruptions. They include pumice clasts and glassy lavas of high-silica dacite and rhyolite compositions (whole rock). With a single exception, they represent the two dominant compositional rock series of Iceland: tholeiitic and transitional alkalic [transitional between tholeiitic and alkali series; *Jakobsson et al.*, 2008]. We did not sample the alkalic series, whose peralkaline compositions lead to little or no zircon in volcanic rocks because of its much higher solubility in peralkaline melts. The sample that does not conform to the standard compositional series is a calc-alkaline dacite from the 11 to 12 Ma Króksfjördur central volcano, the only known locality in Iceland at which such compositions are observed [*Pedersen and Hald*, 1982; *Jónasson et al.*, 1992; *Willbold et al.*, 2009]. Samples range from phenocryst-poor to phenocryst-rich (<5 to >30%). In addition to zircon, all have plagioclase as the dominant phenocryst, along with clinopyroxene and Fe-Ti oxides (magnetite-ulvöspinel ± ilmenite); apatite is present in almost all samples and fayalitic olivine in most tholeiitic and transitional alkalic samples, and sample ITHn (Torfajökull) contains alkali feldspar and minor amphibole. The calc-alkaline sample from Króksfjördur, IIKK, is especially phenocryst-rich (>30%) and is distinguished by abundant hornblende. Silica concentrations and A/CNK of whole rocks range, respectively, from 67 to 75 wt% (oxides normalized to 100%) and 0.88–0.97, and of glasses range, respectively, from 73 to 79 wt% and 0.96–1.12. Excluding the Króksfjördur sample, whole rocks and glass are Zr-rich (450–920 and 460–800 ppm, respectively). Króksfjördur sample IIKK whole rock and glass Zr concentrations are 180 and 120 ppm. Using glass compositions, zircon saturation thermometry yields temperatures of 850–940°C for tholeiitic and transitional alkalic samples, using the calibration of *Boehnke et al.* [2013]; or, alternatively, 880–950°C using the calibration of *Watson and Harrison* [1983]. The zircon saturation temperature for Króksfjördur calc-alkaline glass is 720°C (*Boehnke et al.*, 2013; 770°C using *Watson and Harrison* [1983]).

The three MSH samples span the eruptive stages of the volcano, from the late Ape Canyon stage (oldest) to the most recent Spirit Lake stage [*Clynne et al.*, 2008; *Claiborne et al.*, 2010]. These are weakly peraluminous (A/CNK 1.00–1.06), dacitic pumices (66–68 wt% SiO_2),

Table 1.1 Characteristics of Samples

Sample	Volcanic Unit	Eruption Age[a]	Setting	Compositional Affinity	Phenocryst Assemblage[b]: plag + FeTi ox + zrc + …	WR SiO_2 (wt%)	WR A/CNK	Glass SiO_2 (wt%)	Glass A/CNK	Zr in glass (ppm)	Zirc sat *T*, C[c]	Ti_{zircon} ppm, range
Iceland												
IOHN-1 (pumice)	Öræfajökull central volcano	654 y (1362 AD)	Öræfajökull Volcanic Zone (off-rift)	Transitional tholeiitic-alkalic	ol + cpx	72.4	0.91	73.5	0.99	790	929; 945	9–29
ITHn (lava)	Torfajökull central volcano	1145 y (871 AD)	Eastern Volcanic Zone (propagating rift)	Transitional tholeiitic-alkalic	afs + ol + cpx + hbl + ap	67.0	0.88	74.6	0.97	577	885; 910	12–21
IETR (lava)	Torfajökull central volcano	67 ka	Eastern Volcanic Zone (propagating rift)	Transitional tholeiitic-alkalic	cpx + zrc + ap	72.0	0.92	77.6	0.96	801	939; 952	7–50
IHB (pumice)	Hekla central volcano	858 y (1158 AD)	Eastern Volcanic Zone (propagating rift)	Transitional tholeiitic-alkalic	ol + cpx + ap	68.8	0.95	72.9	1.01	443	855; 910	7–30
IEKG (lava)	Krafla central volcano	~100 ka	Northern Volcanic Zone (rift)	Tholeiitic	ol + cpx + ap	74.2	0.92	76.7	0.98	468	867; 893	10–29
IEKlT (lava)	Kerlingarfjöll central volcano	279 ka	Mid-Iceland Belt	Tholeiitic	cpx + ap	74.9	0.97	79.0	1.12	461	895; 909	9–15
IIKK (lava - cryptodome)	Króksfjördur central volcano	11.5 Ma	Mid-Miocene rift?	Calc-alkaline	hbl + cpx + ap	70.3	0.93	77.9	1.03	119	721; 769	3–16
Mount St. Helens (MSH)												
SHL08-21Z	Cougar stage	24 ka	Subduction zone	Calc-alkaline	hbl + opx + ap	68.3	1.02	74.3	1.01	50	639; 703	3–18
SHL08-26Z	Ape Canyon stage	54 ka	Subduction zone	Calc-alkaline	bio + hbl + qtz + cum + ap	66.4	1.06	76.6	1.08	55	654; 713	2–20
SHL08-34Z	Spirit Lake stage	3.5 ka	Subduction zone	Calc-alkaline	cum + hbl + ap	65.6	1.00	75.3	1.09	93	696; 751	3–20
Colorado River Extensional Corridor (CREC)												
HRL21	Highland Range volcanic sequence	16.0 Ma	Incipient continental rifting	High-K Calc-alkaline	qtz + afs + bio + sph	77.4	1.04	77.7	1.04	80	681; 738	5–13
HRL27	Highland Range volcanic sequence	16.6 Ma	Incipient continental rifting	High-K Calc-alkaline	afs + bio + cpx + ap	67.9	0.95	75.5	1.09	276	808; 847	16–32
KPST01	Peach Spring Tuff	18.8 Ma	Incipient continental rifting	High-K Calc-alkaline	afs + bio + hbl + sph + chev	75.1	0.97	76.8	1.01	144	731; 783	6–23

[a] Iceland ages from *Carley et al.* [2011, 2014]; MSH ages from *Clynne et al.* [2008]; CREC ages from *Colombini* [2009] and *Ferguson et al.* [2013].

[b] afs, alkali feldspar; ap, apatite; bio, biotite; chev, chevkinite; cpx, clinopyroxene; cum, cummingtonite; FeTi Ox, magnetite ± ilmenite; hbl, hornblende; ol, Fe-rich olivine; opx, orthopyroxene; plag, plagioclase; and zrc, zircon.

[c] Zircon saturation temperatures (based on glass (melt) compositions) (shown as *Boehnke et al.* [2013] and *Watson and Harrison* [1983]).

representing typical evolved MSH magma [*Clynne et al.*, 2008]. Less silicic samples failed to yield zircon, and only the pumice samples provided the fresh glass needed for this study. MSH-erupted magmas were generally more evolved in composition, wetter, and cooler early in its history, shifting to drier, hotter, and more mafic in the past ~20 kyr [*Clynne et al.*, 2008], though the zircons record these hotter more mafic compositions in the subvolcanic system as early as 100 ka [*Claiborne et al.*, 2010]. The three samples are from an Ape Canyon stage pyroclastic flow, ~54 ka (SHL08-26Z); a Cougar Stage two-pumice pyroclastic flow, ~24 ka (SHL08-21Z); and the Yn tephra from the Spirit Lake stage, ~3510 ybp [SHL08-34Z; *Clynne et al.*, 2008]. Samples are phenocryst rich, with dominant plagioclase, lesser hornblende, and accessory zircon, apatite, ilmenite, and magnetite. The oldest sample (SHL08-26Z) also contains biotite, quartz, and sparse cummingtonite. The Cougar stage sample (SHL08-21Z) is a light-colored pumice clast from a two-pumice, hypersthene-bearing pyroclastic flow. The Yn tephra (SHL08-34Z) contains cummingtonite, commonly rimmed with hornblende. Silica concentrations in glasses (74–77 wt%) are much higher than in whole rocks A/CNK is similar (1.01–1.09). Whole rocks and glasses are relatively Zr poor (110–130 and 50–90 ppm, respectively). Using glass compositions, zircon saturation thermometry yields temperatures of 640–700°C (*Boehnke et al.*, 2013; 700–750°C by *Watson and Harrison* [1983]).

The three samples from the CREC, described previously by *Colombini et al.* [2011] and *Pamukcu et al.* [2013], include one high-silica rhyolite pumice clast from a supereruption deposit and two lavas (high-Si rhyolite, high-Si dacite) from modest-volume flows. All erupted during the early stages of Miocene extension within mature continental crust in the southwestern USA. Zirconium concentrations range from 90 to 400 ppm (whole rock) and 80–276 ppm (glass), and zircon saturation temperatures based on glass compositions from 680 to 810°C (*Boehnke et al.*, 2013; 740–850°C using *Watson and Harrison* [1983]).

1.3. METHODS

1.3.1. Kds from Zircon and Glass: Approaches

We determine what we consider to be the most robust possible Kds by analyzing the elemental compositions of host glass and the outermost part of zircon crystals in volcanic samples. Assuming that the analyzed zircon and glass represent zircon and melt that were in equilibrium with each other, the zircon/glass elemental ratios represent true Kds. In practice, this entails (i) analyzing zircon rims (outermost analyzable portions of polished interiors; Fig. 1.2a,b) or surfaces (shallow pits on exposed crystals faces; Fig. 1.2c) by SHRIMP-RG (see below); (ii) critically

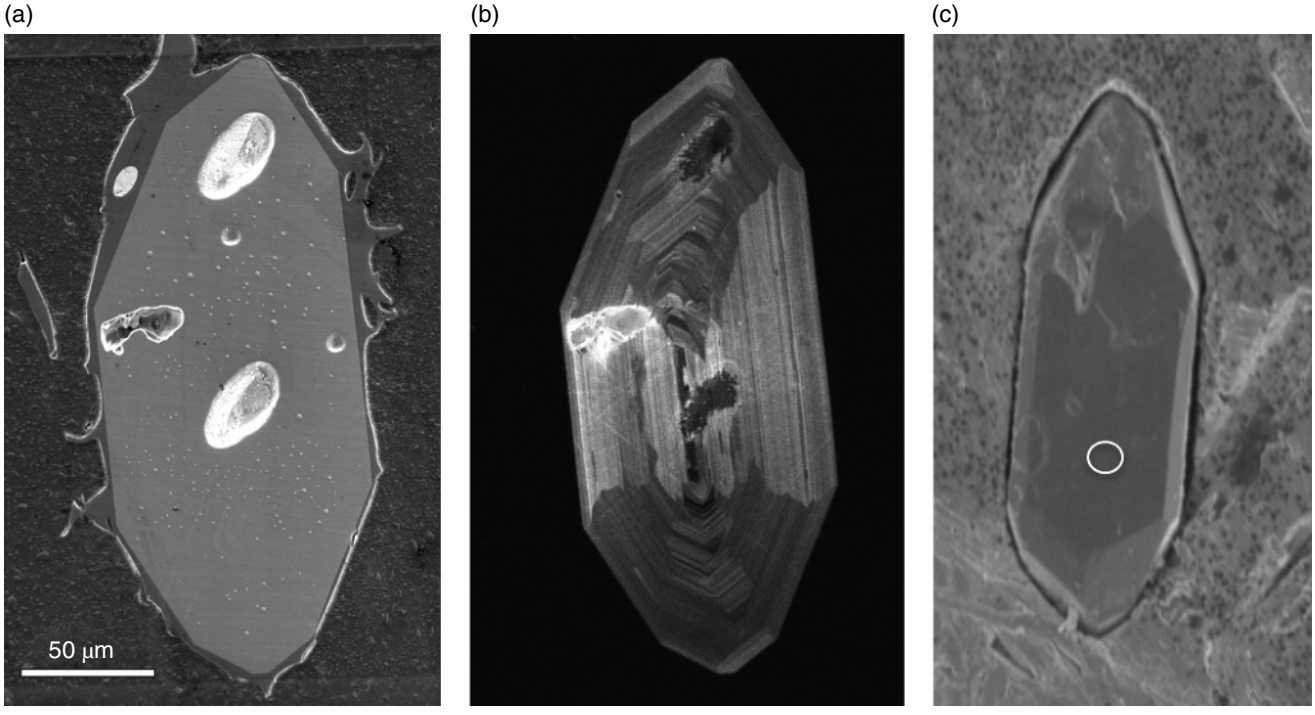

Figure 1.2 Zircons from MSH. White bar is 50 μm. (a) Scanning electron image of a polished zircon with adhering glass. SHRIMP analysis pits shown in the core and rim. (b) Cathodoluminescence image of the polished zircon interior shown in (a). (c) Scanning electron image of a zircon pressed into Indium. The circle indicates the location of a SHRIMP analysis of the "surface" composition.

evaluating and culling the data to eliminate points that overlapped small inclusions as well as otherwise obvious outliers, and using the mean composition of remaining analyses to estimate the elemental concentrations of zircon crystals equilibrated with host melt; (iii) analyzing glass by laser ablation inductively coupled plasma mass spectrometry (LA-ICP-MS), again culling and averaging the data (see below); and (iv) calculating Kds as the ratio of elemental concentration in zircon over concentration in glass.

1.3.2. Surface and Conventional Rim and Analysis by SHRIMP-RG

Zircon separation from all rock samples followed procedures described in *Claiborne et al.* [2010]. For Iceland samples, our methods were conventional for SHRIMP-RG analysis (or SIMS in general), essentially the same procedures as were used for the CREC samples [*Colombini et al.*, 2011; see also *Padilla and Gualda*, 2016]. We mounted up to 50 zircons from each sample in epoxy, and ground and polished mounts near the center of the grains. Mounted grains were imaged in reflected light on a petrographic microscope and by cathodoluminescence (CL) on the JEOL JSM 5600 scanning electron microscope at the USGS/Stanford Microanalytical Laboratory and analyzed for trace elements (~15 μm spot) following *Grimes et al.* [2015] and age by U-Th and/or U-Pb (~30 μm spot) following *Claiborne et al.* [2010].

To estimate most of our Kds, we used trace element analyses of rim zones that were placed as close to the edge as possible. Kds calculated using this conventional analytical procedure are not ideal. With zircon's very slow growth rates [e.g., *Watson*, 1996] and potential pauses in growth, the ~15 μm represented by conventionally analyzed zircon rims can encompass thousands of years, or more, of zircon growth, and compositions may be unrelated to the final host melt. This is further complicated at MSH, likely similar to many other systems, where each eruption extracts zircons that have been stored beneath the volcano for a range of time in various melt compositions; few grains are entirely cognate to the melt in which they erupt [*Claiborne et al.*, 2010]. Imaging of these samples by X-ray tomography showed zircon grains hosted within other crystals as well as within glass [*Gualda et al.*, 2010]; enclosure within other grains is undoubtedly common.

To minimize the limitations of conventional rim analysis as a proxy for zircon in equilibrium with melt, we employed a novel, more rigorous approach to the three MSH samples: we selected zircon crystals with adhering glass and analyzed their surfaces (crystal faces). The advantages of this procedure are that only the outermost 1–2 μm of the crystal is included in the zircon analysis, and we can be confident that the surface was in contact with melt immediately prior to eruption. Zircon grains were immersed in fluoroboric acid, dissolving any adhering glass. Intact crystals were then mounted in Indium, with crystal faces exposed and horizontal, and imaged as with conventional mounts. Exposed zircon faces were then analyzed by SHRIMP-RG following procedures described above for trace elements, followed by U-Th and/or U-Pb (Fig. 1.2c). To improve confidence that we were determining Kds for true cognate zircon-glass pairs, we used only surfaces that yielded ages consistent with time of eruption. For comparison, we also analyzed grains from the same samples by conventional methods (polished cross section; Fig. 1.2b).

Ages were determined by U-Pb and/or U-Th analysis for all samples, but are reported herein only for the three samples from MSH. For these samples, uranium-thorium isotopic compositions were collected first, followed by U-Pb compositions for spots that proved older than ~200 ka by U-Th analyses. Spots for geochronology (~30 μm diameter) were selected to correspond to trace element analysis locations, where possible. U-Th model ages reported for MSH zircon are calculated following procedures described in *Claiborne et al.* [2010].

1.3.3. Glass Analysis

For glass analyses, polished thin sections were coated in carbon. They were then imaged and major element oxide concentrations were determined by quantitative energy dispersive X-ray spectrometry (EDS) analysis using a LaB_6 Tescan Vega 3 LMU SEM equipped with an Oxford X-max 50 mm^2 EDS system at Vanderbilt University. Analyses were conducted with 15 kV electron beam acceleration and maximum beam intensity, optimized using copper tape. Data were acquired and processed using the Oxford software Aztec. Following procedures described in *Pamukcu et al.* [2015], we analyzed USGS standard RGM-1 daily to evaluate accuracy and reproducibility of our results. Mean values for concentrations of the eight oxides reported by *Pamukcu et al.* [2015] for 55 analyses of USGS standard RGM-1 (SiO_2, Al_2O_3, FeO(t), MgO, CaO, Na_2O, K_2O, TiO_2; MnO and P_2O_5 were very near or below detection) differed from preferred RGM-1 values by ≤0.12 wt% and standard deviations were ≤0.13 wt%. Our results during this study were essentially identical to those of *Pamukcu et al.* [2015]. We determined concentrations of trace elements in glass by LA-ICP-MS using a Photon Machines Excite 193 nm HelEx laser ablation unit connected to a Thermo Scientific iCapQ ICP-MS at Vanderbilt University. We set the laser settings to yield a fluence of ~5.9 J/cm^2, at a repetition rate of 10 Hz, with

He (total flow rate of 0.720 LPM between two cells) as the carrier gas. Each analysis began with 20 s of blank acquisition, followed by 60 s of ablation and 10 s of wash-out time to allow the measured values to return to blank levels. Laser spot size of 50 μm^2 was used to provide adequate sample to measure low-concentration elements (e.g., heavy REE (HREE)), while still avoiding crystals within the glass. We measured a total of 57 analytes during each analysis. For every 20–30 measurements of unknowns, we analyzed four primary (for calibration) and secondary (treated as unknowns) standards to evaluate the precision and accuracy of the results. We used *NIST 610*, *612*, and *614* glasses [*Pearce et al.*, 1997; *Kurosawa et al.*, 2002; *Jochum et al.*, 2011] and *USGS rhyolite standard RGM-1* [*Abbey*, 1983; *Govindaraju*, 1994; *Roelandts and Gladney*, 1998] fused glass. *NIST 610* was used as the primary standard, whereas the others were used as secondary standards. Results obtained using secondary standards, particularly RGM-1, are typically within 10% of expected values for reported elements. Glass compositions in several samples were determined using ^{156}Gd, which suffers from interference with Ba. In these cases, Gd glass concentrations and Kds are not reported.

We used *Glitter* [*Griffin et al.*, 2008] to reduce the LA-ICP-MS data. We carefully reviewed and culled individual analyses, looking for evidence that the analyzed volume had encountered significant alteration or crystals. The former, marked, for example, by low Na or high Mg, was rare; the latter, indicated by anomalously high concentrations (for glass) of crystal-compatible elements, for example, Ca, Al, Sr, or Ba (feldspars) or REE, U, Th, Zr, or P (accessory minerals), was rare to common. Suspicious "glass" analyses were rejected; at least 10, and generally more than 20–25, out of ~30 total analyses remained, which were then averaged to yield the best estimate of the concentrations of each element in clean, fresh glass for each sample.

1.3.4. Constraining Magma Temperatures from Zr in Melts and Ti in Zircon

We constrain temperatures at which analyzed zircon rims and surfaces crystallized using two independent measured values: Zr in the glass (melt) and Ti in the zircon. Because of its presence, we infer that the melts were saturated in zircon, and further that Ti in the zircon reflects equilibrium with those melts. These inferences are especially strongly supported where eruption-age zircon surfaces have adhering glass (see above).

Zirconium concentration in silicic melts correlates positively, and closely, with temperature. This is a consequence of the facts that silicate melts are saturated in zircon at or near 70 wt% SiO_2 and remain so to their solidi and that saturation concentrations of Zr decline sharply as temperature falls [e.g., *Hanchar and Watson*, 2003; *Miller et al.*, 2003]. This relationship has been quantified and becomes central to the study of silicic magmatism through development of zircon saturation thermometry [*Watson and Harrison*, 1983]. *Watson and Harrison* [1983] demonstrated that, in addition to temperature, major element composition influences Zr concentration required for zircon saturation of melts; this effect is substantial, but, because zircon-saturated melts do not vary greatly in composition (mostly high in silica, mildly metaluminous to mildly peraluminous), the Zr versus *T* correlation for saturated melts remains very strong (cf. Fig. 1.8a). Importantly, water content (above ~2 wt%) is less influential. Recent work has attempted to update and improve the original Watson and Harrison calibration [*Baker et al.*, 2002; *Boehnke et al.*, 2013; *Gervasoni et al.*, 2016]. All yield results that are broadly consistent with each other and with *Watson and Harrison* [1983], but in detail they differ significantly. In investigating relationships between Kds and temperature in this paper, we present results calculated using the *Boehnke et al.* [2013] calibration, which is the direct descendant of *Watson and Harrison* [1983], using glass compositions that we determine by SEM-EDS and LA-ICP-MS. The correlations that we find are evident using any of the calibrations of the zircon saturation thermometer, or simply using Zr concentration alone as a proxy for temperature.

Titanium concentration in zircon has also been shown to be sensitive to temperature (the *T* at which zircon was growing from melt) [e.g., *Watson and Harrison*, 2005; *Hofmann et al.*, 2013]. The now widely used Ti-in-zircon thermometer requires a_{TiO_2} and a_{SiO_2} as well as Ti concentration of the zircon [*Ferry and Watson*, 2007]. Activity of SiO_2 usually is close to unity (quartz-saturation) for zircon-saturated melts. Activity of TiO_2, however, is highly variable and difficult to evaluate confidently in most cases [e.g., *Reid et al.*, 2011; *Ghiorso and Gualda*, 2013; *Pamukcu et al.*, 2013], especially for melts from which interior zircon zones grew. Uncertainties on the order of ±50°C in Ti-in-zircon temperature estimates are expected for detrital zircons and zircon cores, where a_{TiO_2} during zircon growth is essentially unconstrained [*McDowell et al.*, 2014]. Furthermore, recent sub-micron-scale study of Ti in zircon by NanoSIMS calls into question reliable quantitative application of Ti-in-zircon thermometry [*Hofmann et al.*, 2014], in part because of micron-scale "hot spots" with up to 40 times the Ti concentration of host zircon that were observed in some zircon grains [*Hofmann et al.*, 2009]. In this paper, we demonstrate that Ti concentration in zircon is invaluable as a semi-quantitative

indicator of temperature of crystallization, but because of the inherent uncertainties, we do not rely on quantified Ti-in-zircon temperatures.

1.4. RESULTS: CALCULATED ZIRCON Kds

In a general sense, $Kds^{zircon/glass}$ for all samples show very similar patterns (Table 1.2, Fig. 1.3). Uranium (6-150) and Th (2-50) are compatible (Kd > 1), with $Kd_U > Kd_{Th}$, and Hf is extremely compatible (400–7000). Light REE (LREE) except for Ce are highly incompatible (La < 0.005; see discussion in section 1.5.2), Ce and middle REE (MREE) are slightly incompatible to mildly compatible, and HREE and Y are highly compatible (e.g., Lu 30-750). The Kd pattern for REE therefore has an extremely steep positive slope that extends over about six orders of magnitude for each sample (this range is greater than reported in most Kd studies; see section 1.5.2), with large positive Ce and modest negative Eu anomalies ($Kd_{Eu}/Kd_{Eu*} < 1$, $Kd_{Ce}/Kd_{Ce*} >> 1$). Niobium is generally incompatible (0.1–1.4). In an absolute sense, Kds for individual elements differ greatly from sample to sample, by well over an order of magnitude, but systematically: in a relative sense, individual samples have uniformly low, intermediate, or high Kd values for practically all elements, and therefore Kd patterns in Figure 1.3 are generally subparallel.

Icelandic zircon Kds are far more variable than those for MSH samples, but, with a single exception, they are much lower (Fig. 1.3). The only high Icelandic Kds, which are similar to those for MSH, are for the lone calc-alkaline sample. Kds for CREC samples generally fall between but span much of the range of the Icelandic and MSH samples. Patterns are for the most part parallel, with mostly subtle exceptions. Cerium and Eu are exceptions for which there is considerable crossover (see section 1.5.4).

Although Hf Kds display variability similar to that of other elements, Zr/Hf ratios of zircon relative to those of glass are relatively uniform: the ratio $Zr/Hf^{zircon/glass}$ (alternatively $Kd^{Zr,zircon/glass}/ Kd^{Hf, zircon/glass}$) ranges from 1.15–1.55 for new data for Iceland and MSH (mean 1.34), and ranges from 1.57 to 1.75 for CREC data (mean 1.67; from *Colombini et al.* [2011] (Fig. 1.4a)). We are more confident in the new data and suggest 1.34 as a useful approximation for this ratio. Other elemental Kd ratios of interest, though much less variable than those for individual elements, show considerable spread. $Th/U^{zircon/glass}$ ranges from 0.06 to 0.3 (mean 0.19; Fig. 1.4b). REE Kd ratios ($MREE^{zircon/glass}/HREE^{zircon/glass}$) vary by factors that correlate with atomic number: $Sm^{zircon/glass}/Lu^{zircon/glass}$ by 8, $Dy^{zircon/glass}/Lu^{zircon/glass}$ by 3 (Fig. 1.4c). This is evident in the steeper REE slopes for higher-Kd samples and the greater spread in Kds for HREE than for LREE (Fig. 1.3).

1.5. DISCUSSION AND IMPLICATIONS

1.5.1. New Estimated Zircon Kds: Comparison to Published Estimates

The relative Kds (Kd patterns) presented in Table 1.2 and Figure 1.3 are in a general sense consistent with those that have been proposed over a span of almost five decades (Fig. 1.1). That is, they reveal a steady rise in Kd from LREE to HREE; U and Th are both compatible but U considerably more so; and Hf is extremely compatible (Fig. 1.1). In detail, however, our Kds stand out in several ways from previously published results:

1. Most published work presents only one or a small number of Kd sets for natural samples or experiments (*Rubatto and Hermann* [2007] is an exception), and the Kd sets are in most cases for a limited number of elements, whereas we present data for all REE except Pr (and Pm, which is effectively absent in nature), plus Y, U, Th, Hf, and Nb, for 13 samples of varying composition.

2. Our samples display extreme but systematic variability for all elements: Kd for each element varies by more than an order of magnitude among our samples, but for each sample the pattern is internally consistent: uniformly high, low, or intermediate. To our knowledge, among published studies, only the experiments of *Rubatto and Hermann* [2007] and *Trail et al.* [2012] reveal similar ranges in values.

3. Our LREE Kds and Kd_{LREE}/Kd_{MREE} ratios include the lowest values yet reported, rivaled only by those of *Sano et al.* [2002]: that is, the slopes of the LREE-to-MREE portions of the Kd patterns are steeper than those seen in the literature.

1.5.2. Onuma Diagrams and Lattice Strain Modeling: Evidence for Validity of the REE Kds

The quality of our calculated Kds can be assessed by considering how well they fit to expectations based on the lattice-strain model [*Blundy and Wood*, 1994, 2003], particularly for the REE. The REE show a systematic decrease in ionic radius with increasing atomic number, and Kds are expected to change systematically with ionic radius (r). We generate fits for ln(Kd) as a function of ionic radius for the REE for all of the zircon compositions obtained here (Fig. 1.5). We fit the data to the expression given by *Blundy and Wood* [1994]; the resulting curve is approximately a parabola in ln(Kd) versus r space, which is often referred to as an Onuma diagram [*Onuma et al.*, 1968]. We find best fit curves using the procedure described in *Colombini et al.* [2011], by finding the minimum in the sum of the squares of the differences between observed and expected ln(Kd) allowing three parameters to vary freely: the maximum Kd (D_0), the

Table 1.2 Estimated Zircon Kds from Zircon Rims or Surfaces[a] and Host Glasses

Sample	Ti	Nb	La	Ce	Nd	Sm	Eu	Gd	Tb	Dy	Y	Ho	Er	Tm	Yb	Lu	Hf	Th	U	Zr[b]
HRL21 avg glass	612	23.6	33.6	54.3	12.3	1.82	0.22	1.54	0.24	1.62	12.38	0.38	1.22	0.22	1.69	0.25	3.09	23.43	4.92	80
HRL21 avg rim	6.92	33	0.08	135	0.96	2.05	0.56	20.73	8.35	109.3	1498	50.6	267.1	65.9	607	118.2	11889	1176.9	730.5	480000
Kd	**0.011**	**1.38**	**0.0024**	**2.49**	**0.078**	**1.13**	**2.52**	**13.46**	**34.19**	**67.6**	**121.1**	**134.3**	**218.8**	**293.4**	**359.0**	**475.1**	**3850**	**50.23**	**148.4**	**6034**
HRL27 avg glass	1608	27.4	79.2	146.4	52.7	8.07	1.10	5.73	0.80	4.62	24.76	0.90	2.47	0.34	2.69	0.36	7.73	18.13	3.67	276
HRL27avg rim	26.24	4.82	0.04	54.45	2.84	4.94	2.66	35.48	11.05	120.8	1131	45.2	199.7	41.6	336	61.1	7708	82.0	60.0	480000
Kd	**0.016**	**0.18**	**0.0005**	**0.37**	**0.054**	**0.61**	**2.42**	**6.19**	**13.83**	**26.2**	**45.7**	**50.5**	**80.7**	**122.4**	**125.0**	**172.0**	**997**	**4.52**	**16.3**	**1742**
KPST01 avg glass	775	35.5	52.2	91.3	21.9	3.52	0.18	2.49	0.43	3.08	22.23	0.67	1.98	0.40	2.93	0.49	5.49	36.56	7.96	139
KPST01 avg rim	8.94	12.41	0.14	79.83	1.07	2.18	0.56	16.93	6.20	76.7	948	33.5	166.1	38.3	335	62.6	11165	313.9	238.7	480000
Kd	**0.012**	**0.35**	**0.0027**	**0.87**	**0.049**	**0.62**	**3.09**	**6.79**	**14.52**	**24.9**	**42.7**	**50.1**	**83.9**	**95.5**	**114.4**	**126.9**	**2033**	**8.58**	**30.0**	**3449**
SHL21Z avg glass	790	6.1	13.4	22.6	7.8	1.36	0.68	0.93	0.16	0.84	4.54	0.16	0.42	0.06	0.44	0.06	1.78	4.35	2.31	50
SHL21Z avg surface	5.10	3.72	0.01	9.99	1.02	2.78	1.14	24.08	7.69	79.4	758	29.4	129.8	28.0	237	45.2	11009	55.2	158.8	480000
surface Kd	**0.006**	**0.61**	**0.0008**	**0.44**	**0.131**	**2.05**	**1.66**	**25.79**	**48.41**	**94.6**	**166.8**	**180.5**	**312.3**	**447.7**	**534.0**	**752.5**	**6185**	**12.69**	**68.9**	**9644**
SHL26Z avg glass	558	5.1	18.6	33.4	13.6	2.17	0.52	1.48	0.22	1.08	6.23	0.21	0.56	0.09	0.61	0.10	1.90	5.17	2.45	55
SHL26Z avg surface	7.45	1.67	0.07	6.80	0.29	0.84	0.52	10.10		46.5	478		101.5		229	48.1	12196	30.2	221.1	480000
surface Kd	**0.013**	**0.32**	**0.0040**	**0.20**	**0.021**	**0.39**	**1.00**	**6.83**		**43.2**	**76.7**		**179.7**		**374.2**	**488.2**	**6424**	**5.84**	**90.1**	**8699**
SHL34Z avg glass	793	5.6	15.7	30.1	13.5	2.41	0.59	1.67	0.24	1.26	6.56	0.23	0.60	0.09	0.63	0.09	2.63	3.71	1.57	93
SHL34Z avg surface	3.36	3.73	0.01	8.68	0.39	1.41	0.63	14.54	5.35	62.1	771	25.8	113.9	25.2	224	46.0	11841	39.3	155.1	480000
surface Kd	**0.004**	**0.67**	**0.0007**	**0.29**	**0.029**	**0.58**	**1.08**	**8.68**	**22.20**	**49.4**	**117.5**	**111.1**	**189.2**	**283.5**	**353.0**	**484.9**	**4494**	**10.58**	**98.6**	**5153**
IOHN-1 avg glass	1422	75.0	80.7	153.2	80.4	17.88	3.05		3.28	19.67	114.5	4.25	11.70	1.72	11.39	1.60	18.93	10.71	2.87	790
IOHn avg rim	12.06	7.34	0.04	6.49	0.80	2.56	0.91	24.18		111.1	952		182.0		289	46.3	8206	27.2	59.3	480000
Kd	**0.008**	**0.10**	**0.0005**	**0.04**	**0.010**	**0.14**	**0.30**			**5.6**	**8.3**		**15.6**		**25.4**	**28.9**	**434**	**2.54**	**20.6**	**608**
ITHn avg glass	4725	105.7	90.7	174.2	66.0	12.57	1.90		1.92	10.92	58.39	2.29	6.15	0.94	6.22	0.89	15.14	16.47	5.21	576
ITHn avg rim	13.87	28.05	0.12	33.70	6.08	11.83	2.28	107.5	35.40	377.3	3196	137.9	560.0	106.8	801	129.3	9008	237.5	280.1	480000
Kd	**0.003**	**0.27**	**0.0014**	**0.19**	**0.092**	**0.94**	**1.20**		**18.47**	**34.6**	**54.7**	**60.2**	**91.0**	**114.1**	**128.9**	**145.4**	**595**	**14.42**	**53.8**	**833**
IHB avg glass	1187	67.0	78.0	144.9	71.9	15.56	3.22		2.49	14.48	82.44	3.05	8.03	1.23	8.08	1.20	11.49	10.24	2.79	443
IHB avg rim	12.13	7.80	0.05	7.46	2.59	6.94	2.44	59.77		245.8	1839		372.9		576	94.6	9212	57.7	108.3	480000
Kd	**0.010**	**0.12**	**0.0007**	**0.05**	**0.036**	**0.45**	**0.76**			**17.0**	**22.3**		**46.4**		**71.3**	**78.9**	**801**	**5.64**	**38.8**	**1082**
IETR avg glass	2771	154.6	110.5	225.0	95.2	19.17	3.57	18.36	2.82	16.85	88.49	3.44	9.19	1.36	9.28	1.27	20.96	15.62	5.09	807
IETR avg rim	41.90	13.23	0.03	37.83	0.79	2.72	1.34	25.07	8.73	90.3	843	36.1	159.3	32.1	249	42.7	9731	23.8	32.9	480000
Kd	**0.015**	**0.09**	**0.0002**	**0.17**	**0.008**	**0.14**	**0.37**	**1.37**	**3.09**	**5.4**	**9.5**	**10.5**	**17.3**	**23.7**	**26.8**	**33.6**	**464**	**1.52**	**6.5**	**595**
IEKG avg glass	1453	54.3	61.7	131.6	65.2	15.38	1.63	16.48	2.78	17.65	101.6	3.81	10.67	1.62	11.45	1.67	12.63	8.12	2.60	464
IEKG avg rim	13.23	7.54	0.01	5.65	0.66	1.96	0.56	21.45	8.04	97.9	972	39.5	182.5	38.4	319	58.5	9513	22.7	51.4	480000
Kd	**0.009**	**0.14**	**0.0002**	**0.04**	**0.010**	**0.13**	**0.34**	**1.30**	**2.90**	**5.5**	**9.6**	**10.4**	**17.1**	**23.7**	**27.9**	**35.0**	**753**	**2.79**	**19.8**	**1035**
IEKLT avg glass	1119	77.0	72.3	144.1	67.6	14.85	2.86	15.17	2.43	14.90	80.64	3.11	8.54	1.30	9.12	1.29	13.89	11.60	3.33	473
IEKLT avg rim	11.91	14.55	0.14	11.54	1.07	2.78	0.81	25.24	9.46	113.5	1040	44.4	202.3	41.8	361	58.7	9894	42.9	96.8	480000
Kd	**0.011**	**0.19**	**0.0019**	**0.08**	**0.016**	**0.19**	**0.28**	**1.66**	**3.90**	**7.6**	**12.9**	**14.3**	**23.7**	**32.3**	**39.5**	**45.6**	**712**	**3.70**	**29.1**	**1014**
IIKK avg glass	433	4.4	21.4	33.4	10.4	1.72	0.48	2.11	0.22	1.06	6.29	0.23	0.57	0.09	0.58	0.09	3.31	4.96	1.58	119
IIKK avg rim	4.78	2.5	0.0	17.4	1.3	1.9	1.0	15.7	5.7	66.4	775	27.9	139.0	33.1	309	64.7	11608	141.8	232.8	480000
Kd	**0.011**	**0.58**	**0.0010**	**0.52**	**0.123**	**1.11**	**1.99**	**7.45**	**26.16**	**62.7**	**123.3**	**121.8**	**242.4**	**374.3**	**535.0**	**713.2**	**3505**	**28.62**	**147.7**	**4030**

[a] Zircon surfaces are eruption-age surface only.

[b] Assumed Zr concentration in zircon = 480,000 ppm Zr.

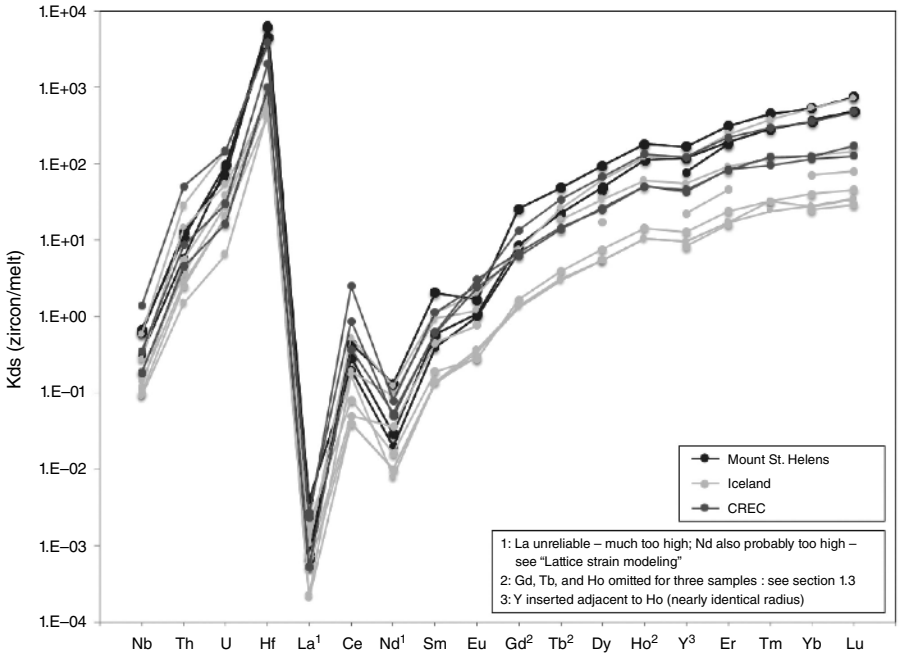

Figure 1.3 Estimated Kds based on zircon surfaces (MSH) and conventional rims in cross section (others). CREC, Colorado River Extensional Corridor, AZ-NV, USA. (*See insert for color representation of the figure.*)

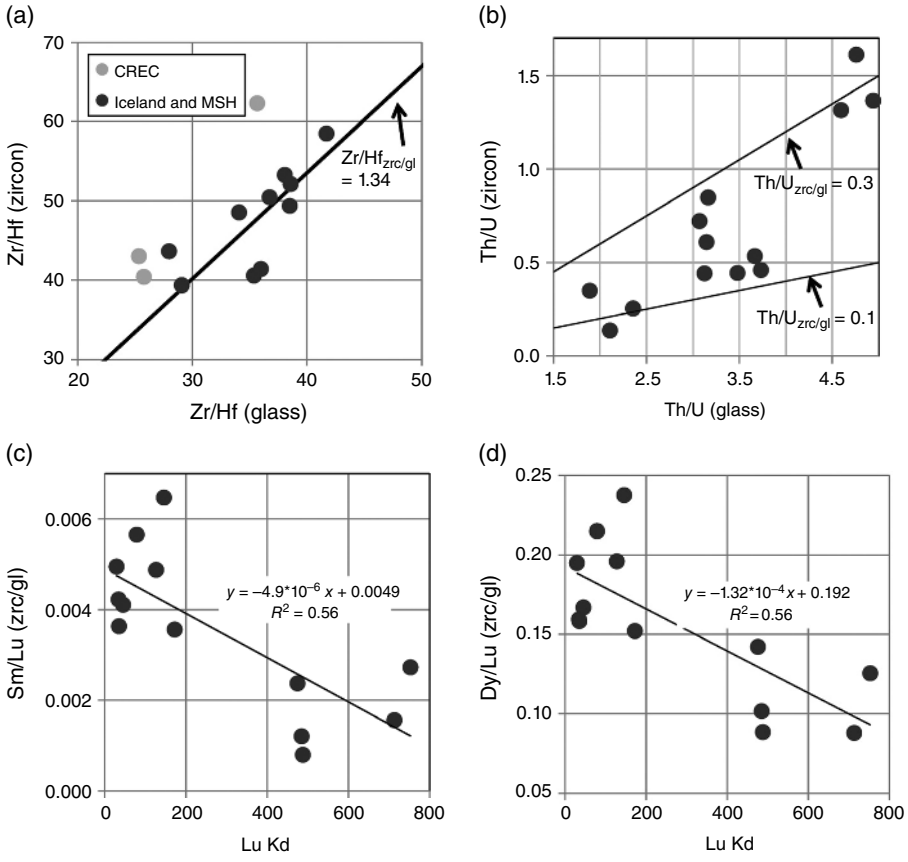

Figure 1.4 Elemental ratios in zircon versus ratios in glass. (a) Zr/Hf (1.34 = mean ratio $Zr/Hf_{zircon}/Zr/Hf_{glass}$); (b) Th/U ($Th/U_{zircon}/Th/U_{glass}$ = 0.1 and 0.3 shown for reference); (c) $Sm/Lu_{zircon}/Sm/Lu_{glass}$ versus Lu Kd, with linear correlation; and (d) Dy/Lu $Lu_{zircon}/Dy/Lu_{glass}$ versus Lu Kd, with linear correlation.

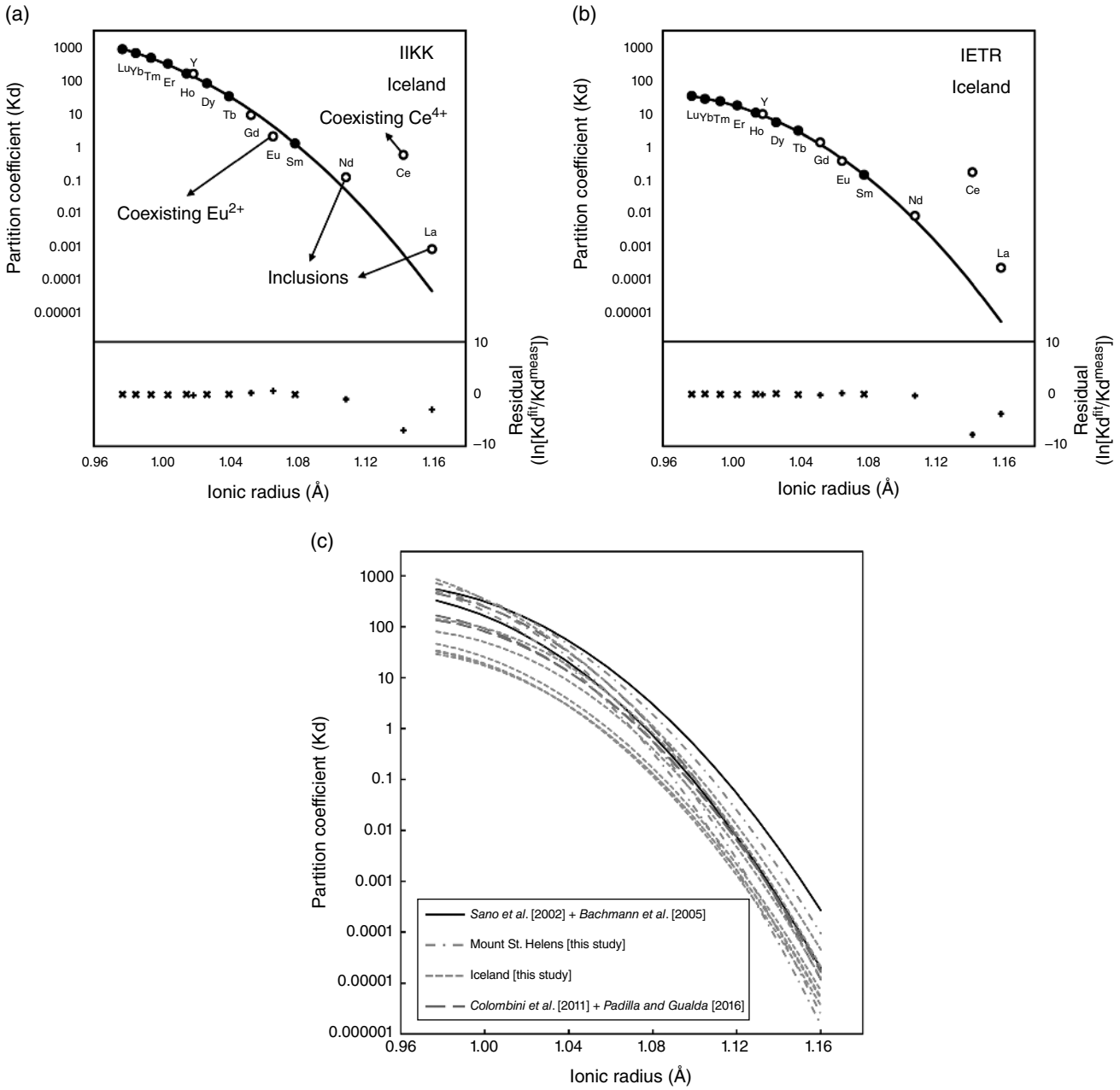

Figure 1.5 (a and b) Onuma diagrams for REE for two Icelandic samples. Top portion of the diagrams shows partition coefficient versus ionic radius for our data (circles); solid line represents best fit curve using the lattice-strain model of *Blundy and Wood* [1994]. Filled circles are included in the calculation of the best fit curves, while open circles are ignored for best fit procedure. Bottom diagram shows residuals between measured and best fit values for each element, with elements included or excluded in best fit calculation indicated by different crosses. Best fit curve fits the included data very well. Note that Eu and Ce are not expected to follow the best fit curve due to the coexistence of two valence states. Extrapolation of the best fit curve to La shows that expected partition coefficients for La are very low, resulting in very low concentrations of La in zircon; measured values are much higher than expected, and probably reflect the presence of small inclusions. This same problem also affects Nd, but to a much lower extent. See text for details. (c) Onuma diagram for REE showing best-fit curves for data from this study and select data from the literature. Best fit curve for the data from *Bachmann et al.* [2005] is based only on Sm, Dy, Er, and Yb due to the lack of data for Tb, Ho, Tm, and Lu. Note that best fit curves are mostly subparallel, and they vary by more than an order of magnitude, particularly for the HREE. Some of the data for MSH show a distinctively steeper slope (more enriched in HREE over LREE).

ionic radius at which the maximum occurs (r_0), and an elastic parameter that controls how tight the curve is (E). Generating best fit curves for REE in zircon has some challenges given three main factors [see *Colombini et al.*, 2011; *Padilla and Gualda*, 2016]:

1. REE patterns in zircon are very steep, with high HREE Kds and very low LREE Kds (see above), which makes the fitting procedure somewhat more difficult given that the maximum of the best fit curve is not necessarily present in the range of available data. The main consequence is that parameters derived from the fitting procedure are not very well constrained.

2. The coexistence of Ce^{4+} and Ce^{3+} and Eu^{2+} and Eu^{3+} causes Kds for Ce and Eu to deviate from the pattern established by the trivalent REE: Ce is more compatible in zircon than would be expected, while Eu is less compatible than expected.

3. LREE, particularly La, have very low concentrations in zircon, which makes their concentrations easily overwhelmed by the presence of minute LREE-rich inclusions. This problem is aggravated by the coexistence of Ce^{3+} and Ce^{4+}, which causes total Ce not to conform to the expected best fit curve.

Due to the considerations above, we do not include in the fit La, Ce, Nd, or Eu; in a few of the analyses, we also exclude Gd due to analytical problems in some of our glass analyses (see above), and we do not include Pr, which is not included in the SHRIMP analyses of zircon. As a result, the fitting procedure only includes HREE and MREE, and we extrapolate the best fit curves to the LREE.

Even though the La Kd values we determined are the lowest among those available in the literature, the best fit curves demonstrate that La Kds are more than an order of magnitude too high. Predicted values for La in zircon are in the range of 0.03–2 ppb, while measured values are in the range 13–140 ppb: resulting observed/predicted La ratios are between 2 and 710. Importantly, there is no correlation between predicted and measured values, showing that La measurements are independent of the intrinsic concentration of La in zircon.

Our fits also show that some Kd values for Nd are higher than expected. The enrichment of measured over predicted Nd values is only in the range of 1.3–4.3, suggesting that inclusions contribute on the order of 50% of the total measured Nd.

The simplest explanation for the anomalies above is that inclusions of minerals and glass affect the measured values, with the effect of inclusions of LREE-rich accessory minerals being particularly acute. The effect is largest for La, which appears in very low concentrations (ppb or lower) in zircon, but it is also detectable for Nd. As an example, apatite typically includes 5000 ppm La [*Padilla and Gualda*, 2016]; with predicted concentrations of ~1 ppb and a pit size of 20 μm diameter and 2 μm depth, a spherical inclusion of <0.5 μm diameter would be enough to generate the largest enrichment observed in our analyses. Rhyolite glass, with typical La concentration on the order of 50 ppm, could contribute enough La if found as a spherical inclusion of only 1.5 μm diameter. We emphasize that such inclusions would be very difficult to identify within zircon crystals.

As we note above, zircon is ubiquitously characterized by strong positive anomalies in Ce concentration due to the coexistence of Ce^{3+} and Ce^{4+} and the low concentrations of Ce^{3+} in zircon; the Ce anomaly has been used as a proxy for oxygen fugacity [e.g., *Trail et al.*, 2012]. One important consequence of the analysis above is that determination of the Ce anomaly (Ce/Ce*: measured total Ce divided by predicted Ce^{3+}) is hampered by the fact that elements commonly used to calculate the predicted Ce^{3+} value (La and Nd) are invariably affected by inclusions. This means that calculation of Ce* requires extrapolation using MREE concentrations, which is likely to yield less precise and accurate results than if La and Nd could be used.

Finally, inspection of our best fit curves (Fig. 1.5b) reveals that best fit curves are significantly steeper (i.e., higher HREE/LREE) for higher Kd samples (e.g., for MSH). This yields a fanning of Kd patterns from low- to high-atomic number. The cause of this difference is not apparent at this point, but we note below that the HREE Kds show the strongest correlation with temperature.

Our modeled best fit Kds are compared with our measured zircon/glass Kds in Table 1.3.

Table 1.3 Best fit Parameters for Curves Describing Relationship Between Kds and Ionic Radius [*Onuma et al.*, 1968; *Blundy and Wood*, 1994] for Samples from This Study and from *Colombini et al.* [2011], *Bachmann et al.* [2005], and *Sano et al.* [2002]

	D_0	E_M^{3+} (GPa)	r_0^{3+} (Å)	T (°C)
Bachmann	695	629	0.95	675
Sano	480	722	0.94	725
HRL21	541	805	0.95	685
HRL27	212	805	0.95	813
KPST01	138	868	0.96	732
IOHN-1	34	906	0.95	928
ITHn	152	969	0.97	884
IHB	89	893	0.96	854
IETR	41	890	0.95	939
IEKG	44	848	0.95	865
IEKLT	60	852	0.95	898
IIKK	2741	530	0.90	721
SHL-21Z	1209	589	0.93	632
SHL-26Z	827	773	0.94	655
SHL-34Z	683	813	0.94	701

Note: Temperatures estimated using *Boehnke et al.* [2013], except for "Sano," for which no data are available for Zr in the glass coexisting with zircon; we roughly estimate 725 °C.

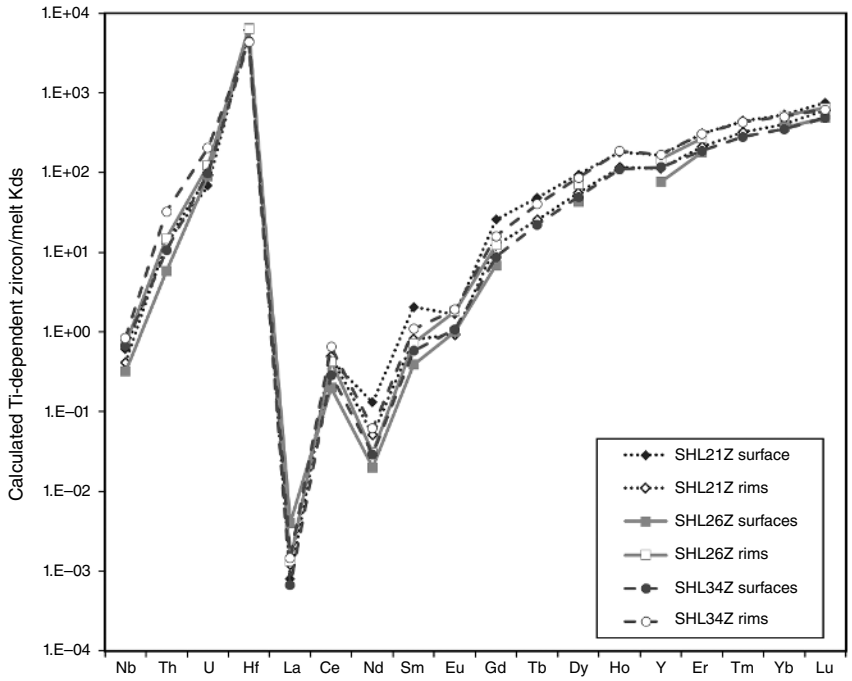

Figure 1.6 Calculated zircon-melt Kds for the three Mount St. Helens samples. Kds calculated from surface analyses are represented by closed symbols, and Kds calculated from conventional rim analyses are represented by open symbols.

1.5.3. Comparing Kds from Eruption-Age Surfaces with Kds from Conventional Rims

Zircon surfaces with adhering glass that yield eruption ages (within error), like those analyzed here from MSH, should provide cognate zircon-glass pairs from which to calculate accurate Kds, as these surfaces represent the last 1–2 μm of growth of zircon from the melt preserved as adhering glass (Fig. 1.2a and c). Our surface analyses reveal compositional variability for individual grains and samples, suggesting that even these surfaces may not all be cognate to the same erupted melt: that is, to the glass preserved within the sample. The variability is, however, relatively limited, and we consider them to offer the most reliable estimates of true Kds.

As discussed in section 1.3, conventional rim analyses of polished grains average at best the outer ~15 μm of growth (weighted toward the center of the spot, ~8 μm in from the surface; Fig. 1.2a). Thus, they integrate a volume of the crystal that may have grown well before the crystal face, from melts that were on average distinctly different in composition from the cognate melt represented by host glass. Thus, Kds calculated from conventional rim analyses might differ substantially from "true" Kds, and differ from each other for a single sample. To evaluate how this affects apparent Kds, we have calculated Kds based on conventional analyses of zircon rims from the same MSH samples as we used for surface analyses.

While the concentrations from surface analyses are slightly more uniform, the calculated Kds based on averages of conventional analyses are similar to those from average surfaces (Fig. 1.6). Among the 51 calculated Kds (16–18 elements, three samples), none differed from surface analysis-based Kds by more than half an order of magnitude (factor of 3), and only 10 differed by more than 0.3 orders of magnitude (factor of 2); of the 10, six are for LREE and two are for Th. The mean discrepancy between surface- and rim-determined Kds is about 0.2 orders of magnitude (factor of 1.7). Although substantial, these discrepancies are small compared to the total ranges in Kds for individual elements (typically about 1.5 orders of magnitude; Fig. 1.3, Table 1.4). We conclude that, although using eruption-age zircon surface compositions paired with host glass data is preferred for determining Kds, conventional zircon rim analyses are adequate for estimating useful Kds.

1.5.4. Possible Controls of Variability of Kds

Extreme variation in equilibrium Kds is presumably controlled by one or more of the intensive parameters that define the magmatic environment of zircon growth: oxygen fugacity, phase composition (that of zircon and melt), pressure, and temperature [*Blundy and Wood*, 2003].

Oxygen fugacity (f_{O_2}) influences partitioning of polyvalent cations: in the case of zircon, it will affect Eu, Ce,

Table 1.4 Comparison of Kds for Three MSH Samples, Calculated Using Eruption-Age Zircon Surfaces Versus Conventional Rim Analyses

	SHL21Z		SHL26Z		SHL34Z	
	Surface	Rim	Surface	Rim	Surface	Rim
Nb	0.61	0.41	0.32	0.72	0.67	0.84
Th	12.7	13.46	5.8	14.93	10.6	32.42
U	68.9	94.10	90.1	122.19	98.6	204.74
Hf	6185	6110	6424	6382	4494	4385
La	0.0008	0.0012	0.0040	0.0013	0.0007	0.0015
Ce	0.44	0.50	0.20	0.43	0.29	0.65
Nd	0.13	0.05	0.02	0.03	0.03	0.06
Sm	2.05	0.81	0.39	0.72	0.58	1.09
Eu	1.66	0.92	1.00	1.81	1.08	1.90
Gd	25.8	12.3	6.8	12.3	8.7	15.9
Tb	48.4	25.8	—	—	22.2	40.1
Dy	94.6	56.0	43.2	72.2	49.4	86.8
Ho	181	117	—	—	111	187
Y	167	114	77	147	118	169
Er	312	212	180	272	189	309
Tm	448	325	—	—	283	431
Yb	534	409	374	514	353	504
Lu	753	600	488	645	485	618

and possibly U [e.g., *Burnham and Berry*, 2012; *Trail et al.*, 2012]. It is the only factor that is likely to substantially disrupt the coherent behavior of the REE and their Kds. In contrast to the typical trivalency of the REE, a large fraction of Eu ions are divalent, and a small but discernible fraction of Ce ions are quadrivalent. As a consequence, partitioning of Ce and Eu in zircon is quite different from that of the adjacent-atomic number REE. Cerium^{4+}, with an ionic radius very similar to that of Zr^{4+}, is many orders of magnitude more compatible than Ce^{3+} [e.g., *Colombini et al.*, 2011], and Eu^{2+}, with a radius that exceeds that of Zr^{4+} by much more than that of Eu^{3+}, is relatively incompatible [*Trail et al.*, 2012]. Thus, zircon invariably exhibits a positive Ce anomaly in its Kd pattern and chondrite-normalized REE pattern ($Ce/Ce^* >> 1$) and generally also has a smaller, negative Eu anomaly. These anomalies, which are sensitive to f_{O_2} [*Trail et al.*, 2012], are evident in our Kds (Fig. 1.3). This sensitivity is demonstrated by the deviations of our Kd patterns from parallelism at Ce and Eu. However, f_{O_2} is unlikely to affect other elements [*Burnham and Berry*, 2012] except perhaps U (charges of 6+ and 4+), and it certainly cannot explain systematic order-of-magnitude variability.

Phase compositions of both crystals and melts undoubtedly can influence Kds [e.g., *Blundy and Wood*, 2003]. Variability in the composition of natural zircon is limited: it is a relatively pure phase, generally comprising at least 97% $ZrSiO_4$ component; Hf is the only substituting element that commonly approaches 10,000 ppm (1 wt%) concentration. Some experimental studies and investigations of naturally occurring zircon indicate that the charge-balancing xenotime substitution ($REE^{3+} + P^{5+} = Zr^{4+} + Si^{4+}$) may play an important role in REE behavior in zircon, but the relationship appears to be complex [e.g., *Hanchar et al.*, 2001; *Hoskin and Schaltegger*, 2003; *Hofmann et al.*, 2009; *Burnham and Berry*, 2012; *Yang et al.*, 2016]. Because apatite typically saturates at higher temperature than and therefore coexists with zircon in magmas [*Harrison and Watson*, 1984], activity of P_2O_5 is generally buffered during zircon crystallization, and we do not see evidence for strong correlation between P and REE in our analyses. Other suggested charge-balancing substitutions involve interstitial 1+ and 2+ cations such as Li^+, H^+, and Mg^{2+} [*Hofmann et al.*, 2009; *Trail et al.*, 2011; *Trail et al.*, 2016; *Yang et al.*, 2016], but to our knowledge no evidence of their influence has been documented, and we suspect that effects on zircon Kds are at most minor and unlikely to be responsible for our observed order of magnitude variabilities.

The fact that coexisting silicate melts of strongly contrasting composition partition trace elements (i.e., that $Kd^{melt\ a/melt\ b}$ differs from unity) requires that melt chemistry must influence mineral/melt Kds, including for zircon [*Watson*, 1976; *Blundy and Wood*, 2003]. However, natural zircon-saturated melt compositions tend to be restricted in composition, and this is certainly true of the samples that we analyzed, all of which have 73–79 wt% SiO_2. Furthermore, zircon Kds for our samples appear to show almost no correlation with SiO_2 or compositional parameters that reflect the melt structural environment (SiO_2; M [*Watson and Harrison*, 1983]; FM [*Ryerson and Watson*, 1987]; A/CNK; NBO/*T* [*Mysen et al.*, 1985]) (Fig. 1.7).

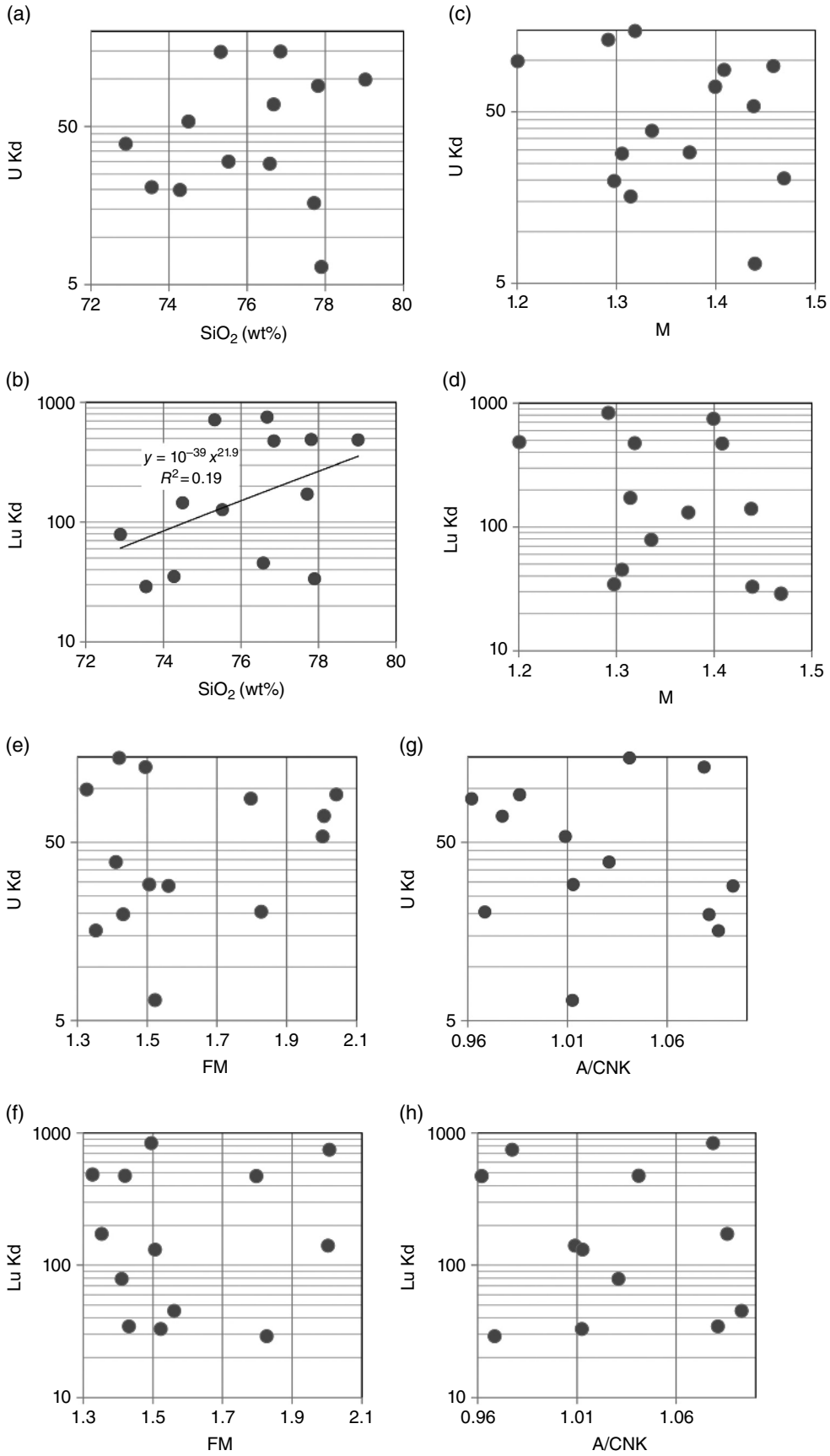

Figure 1.7 $Kds^{zircon/melt}$ versus melt (glass) composition parameters. Only Lu Kd versus SiO_2 shows any correlation. (a) U Kd versus SiO_2; (b) Lu Kd versus SiO_2; (c) U Kd versus M [*Watson and Harrison*, 1983]; (d) Lu Kd versus M; (e) U Kd versus FM [*Ryerson and Watson*, 1987]; (f) Lu Kd versus FM; (g) U Kd versus A/CNK (molecular $Al_2O_3/(CaO+Na_2O+K_2O)$); (h) Lu Kd versus A/CNK; (i) Lu Kd versus NBO/*T* [*Mysen et al.*, 1985]; and (j) U Kd versus NBO/*T*.

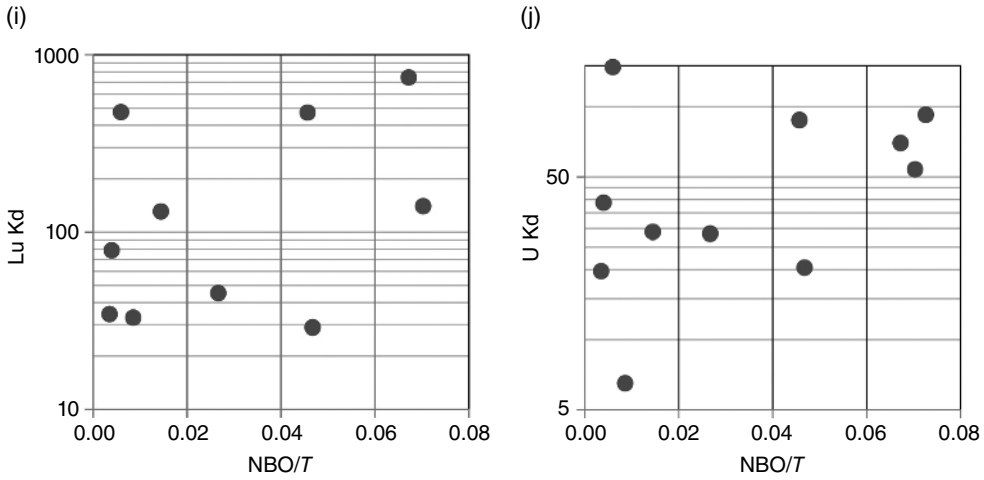

Figure 1.7 (Continued)

Water represents a special case in terms of effects of melt composition. It lowers melting temperature of pure phases and increases their solubility, dramatically so for many phases at elevated pressure. *Wood and Blundy* [2002] and *Blundy and Wood* [2003] discuss the effect of water on Kds of trace constituents. Experimental studies of zircon partitioning have suggested that the water effect on solubility is small, at least for concentrations in the melt of $H_2O > \sim 2$ wt% [*Watson and Harrison*, 1983; *Boehnke et al.*, 2013], but on theoretical grounds such an effect must exist. However, because of the very strong effect that water content has on magma temperature, it is difficult to distinguish the effects of varying H_2O concentration from that of temperature. In our following discussion of apparent temperature effect on Kds, we acknowledge that this effect may in part reflect water.

Pressure undoubtedly influences Kds for minerals generally [e.g., *Blundy and Wood*, 2003], but we doubt that it is responsible for an appreciable part of the variation that we observe in our data. All of the magmas in the volcanic systems that we investigated were stored in the upper crust prior to eruption [~0.1–0.35 GPa; *Claiborne et al.*, 2010; *Colombini et al.*, 2011; *Carley et al.*, 2011; *Pamukcu et al.*, 2013, 2015]. It is highly improbable that this narrow pressure range could have come close to yielding order-of-magnitude variability in Kds.

Temperature is expected to correlate negatively with Kds on thermodynamic grounds [*Wood and Blundy*, 2002], and although we are unaware of any single study of experimental or natural materials that presents full sets of Kds over a range of temperatures, published data for zircon are consistent with this expectation [e.g., *Rubatto and Hermann*, 2007; *Trail et al.*, 2012; *Burnham and Berry*, 2012]. As we show in section 1.5.5, our data set for zircon clearly demonstrates this relationship, and we argue that it is strong enough that it can be used as a practical guide for application of zircon Kds.

Sector Zoning of zircon may result from different partitioning of elements on different faces of a crystal. *Chamberlain et al.* [2014] show that dark sectors in zircons from the Bishop Tuff have up to 45% higher Ti, and are higher in U and Th by up to three times and other trace elements by up to two times the concentration of lighter sector zones. We do not examine sector zoning in our own samples (some MSH and CREC zircon and none of the Icelandic zircons used in this study are sector zoned), but the magnitude of variability shown in *Chamberlain et al.* [2014] is within the variability of our Kds. This gives us confidence that our estimated Kds capture this aspect of natural variability of Kds, and with appropriate caution, can be used to calculate model melts from sector-zoned zircons.

1.5.5. Kd-Temperature Correlation

Zirconium, and zircon itself, provides the information that most practically informs assessment of temperature of zircon growth for the samples in this study. As discussed in section 1.3, Zr concentrations in glasses undoubtedly correlate with zircon-saturated melt temperature, and zircon saturation thermometry provides moderately precise quantitative estimates of temperature. Following the error propagation approach of *Boehnke et al.* [2013], we estimate the precision of our calculated saturation temperatures to be ~±20–40°C (95% confidence); this uncertainty does not take into account any systematic error in the calibration, but systematic error does not affect evaluation of sensitivity of Kds to *T*. Furthermore, temperature also correlates with a quantity directly measurable within the zircon itself, Ti concentration. Figure 1.8 demonstrates correlations among these three parameters. Figures 1.9, 1.10, and 1.11 compare

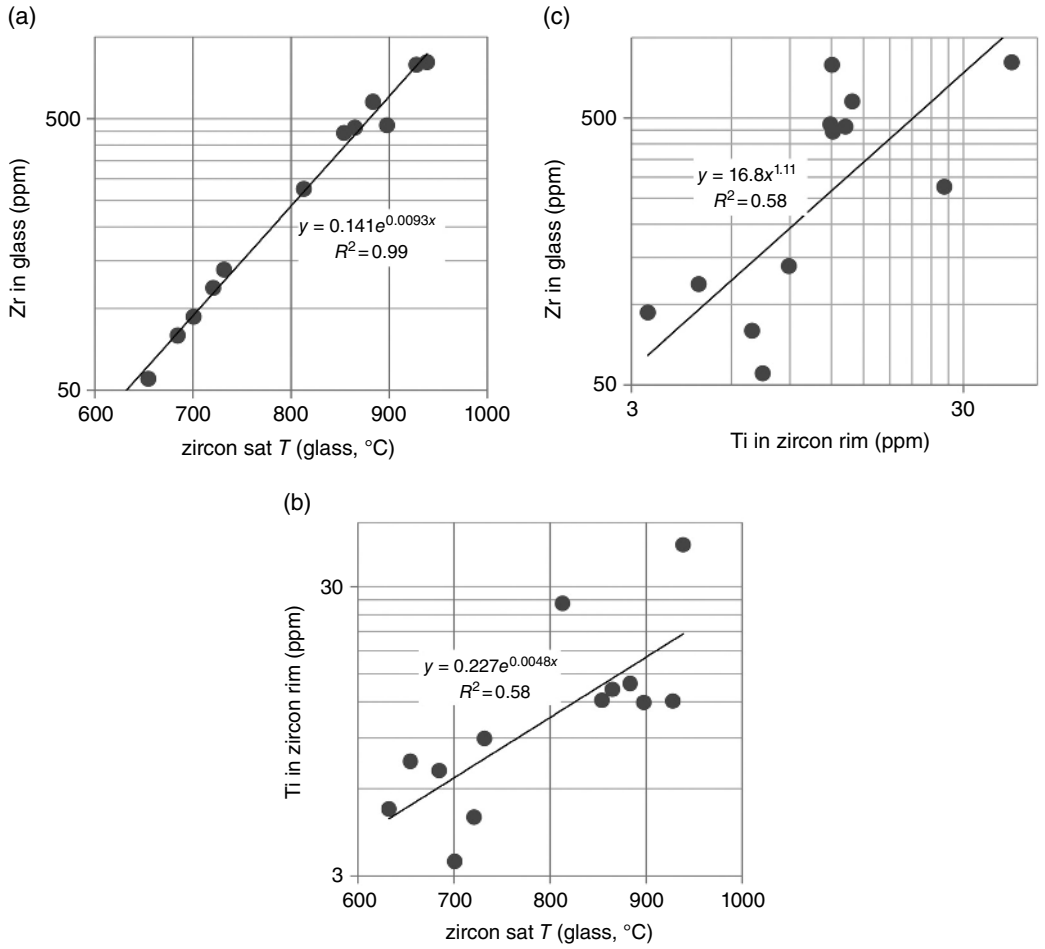

Figure 1.8 Comparisons of temperature-related quantities in zircon and coexisting melt (glass), with correlations. (a) Zr concentration in glass (ppm) versus calculated zircon saturation temperature [*Boehnke et al.*, 2013; based on glass compositions]; (b) Ti concentration in zircon rim or surface (ppm) versus calculated zircon saturation temperature; and (c) Zr concentration in glass (ppm) versus Ti concentration in zircon rim or surface (ppm).

Zr in coexisting glass, zircon saturation temperature based on composition of glass, and Ti concentration in zircon rims and surfaces with calculated Kds. Zircon saturation temperature and Zr concentration are obviously closely related, but we include both because the first is directly measurable, whereas the second is indirect (based upon Zr and other compositional variables and on an experiment-based model) but aims to provide a direct, quantitative estimate of temperature. The correlations are not perfect, but much of the extreme variation in Kds is accounted for, especially by zircon saturation temperature. It is possible that other factors that correlate with temperature (e.g., H_2O content of melt) may play a role, but we conclude that the primary factor responsible for the large ranges in Kds for individual elements in our data set is temperature.

The poorest correlation of the three variables is with Ti in zircon rims, but that relationship has the greatest potential value, as discussed in section 1.6.

1.6. IMPLICATIONS AND APPLICATIONS

1.6.1. Robustness of New Kds in Context of Published Estimates

As Figure 1.1 and the associated discussion indicate, our new Kds fall within the total ranges reported in previous studies and for the most part define similar patterns. However, as noted, our Kd data set is distinguished by extremely low Kds for LREE, at the bottom of the established range, and REE slopes that are as steeply positive as any in the literature.

The excellent fits of REE Kds with reasonable lattice strain models give us confidence in the forms of the patterns for REE Kds, and probably for other elements as well. Evaluations of published Kds further validate our results. The single REE Kd pattern for zircon in *Sano et al.* [2002] matches almost perfectly those that

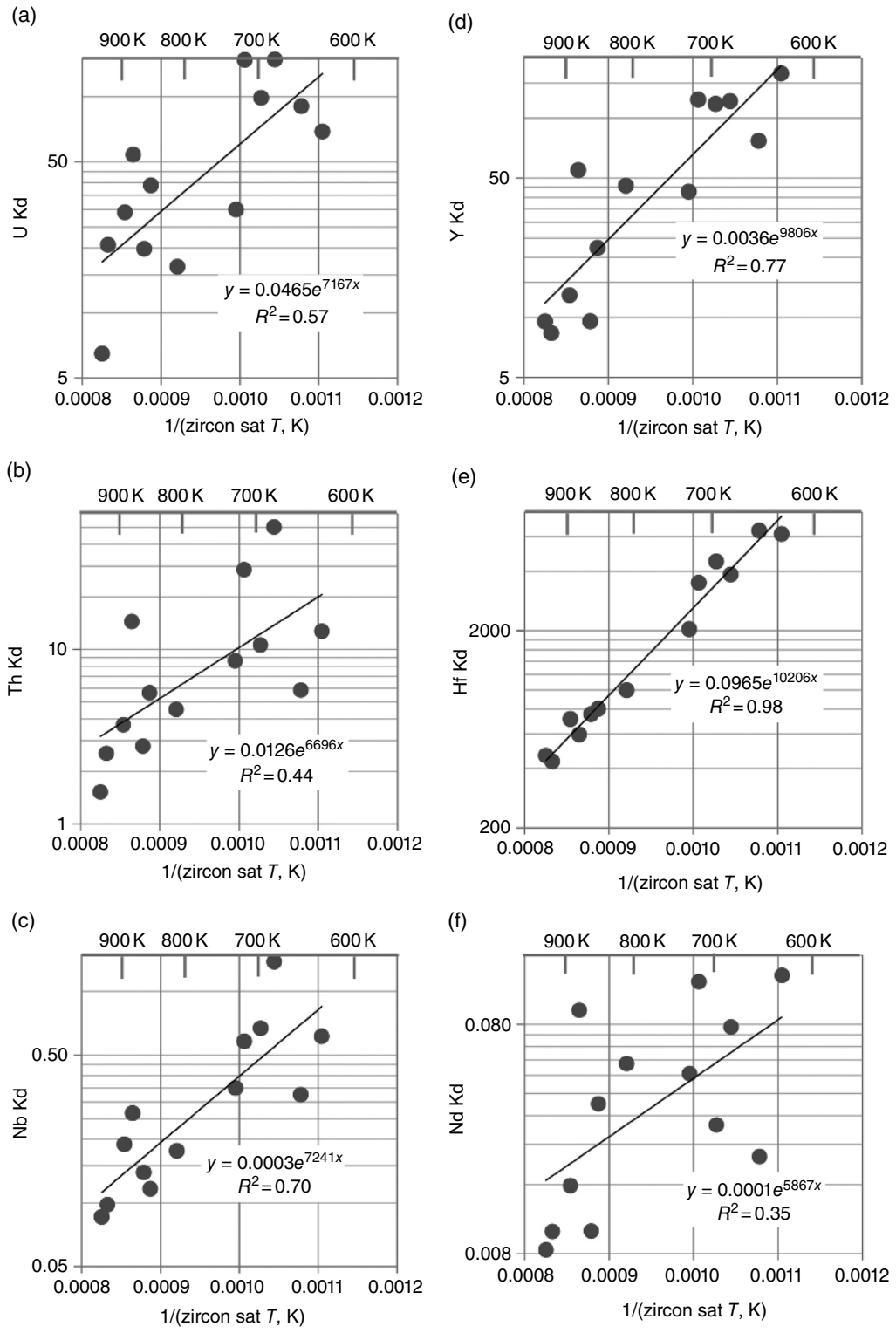

Figure 1.9 $Kds^{zircon/melt}$ versus 1/calculated zircon saturation temperature [*Boehnke et al.*, 2013; based on glass compositions]. (a) U Kd; (b) Th Kd; (c) Nb Kd; (d) Y Kd; (e) Hf Kd; (f) Nd Kd; (g) Sm Kd; (h) Eu Kd; (i) Gd Kd; (j) Tb Kd; (k) Dy Kd; (l) Ho Kd; (m) Er Kd; (n) Tm Kd; (o) Yb Kd; and (p) Lu Kd.

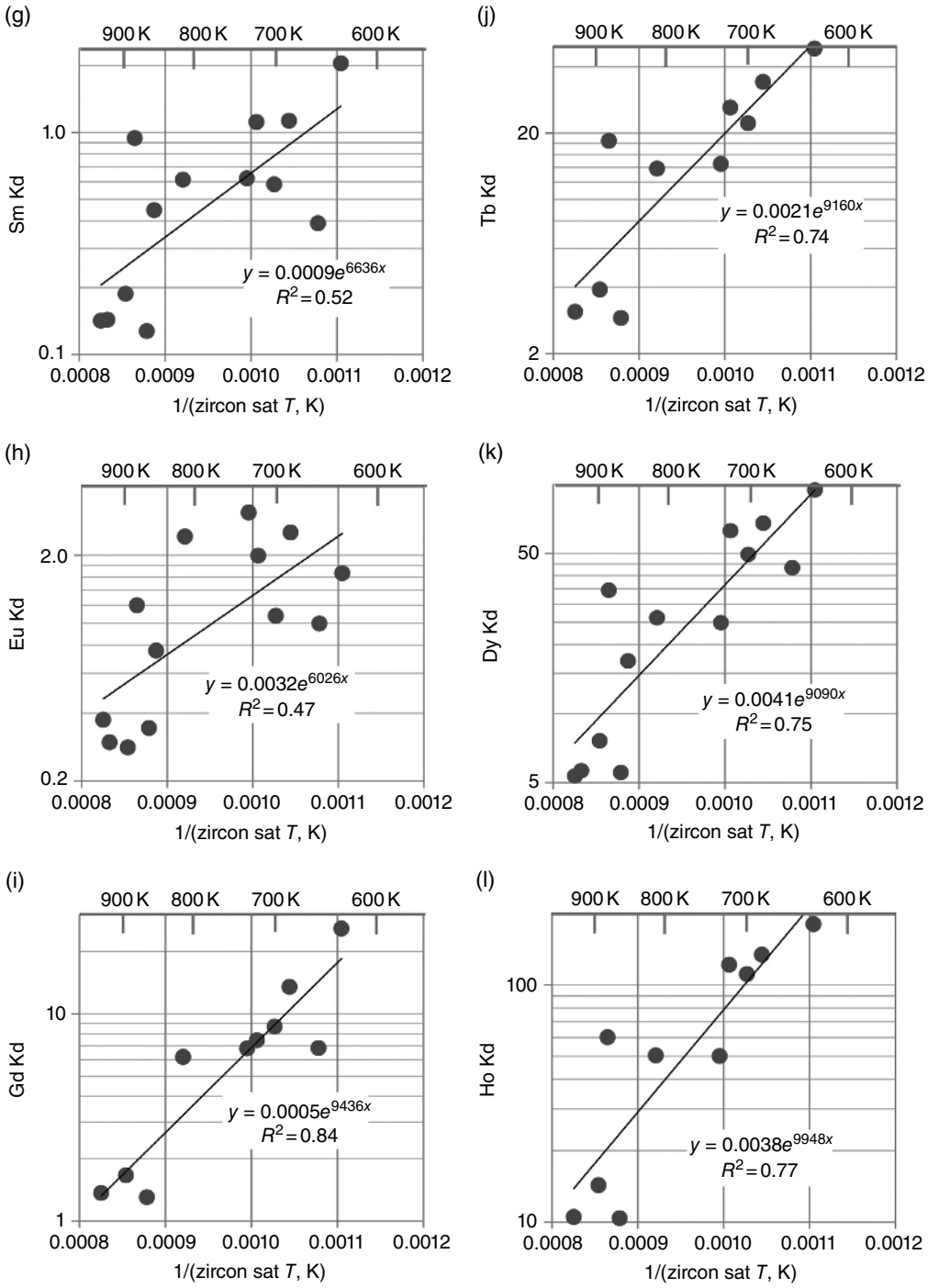

Figure 1.9 (Continued)

we present for relatively low-T samples, as does the single-sample, multi-element zircon Kd data set of *Bachmann et al.* [2005; excluding their higher LREE Kds]. Only *Rubatto and Hermann* [2007; experimental study] systematically present a large number of elemental Kds (Th, U, Zr, Hf; REE from Nd through Lu) for multiple samples or conditions. Their values, ranges of values, and Kd patterns closely match ours and mimic the temperature dependence that we suggest (their T range of 250°C is very similar to ours); their results also indicate steepening of the REE Kd slope with decreasing T. The only published Kds that are uniformly lower than ours are those from *Burnham and Berry* [2012]. Their results are also entirely consistent with ours: their

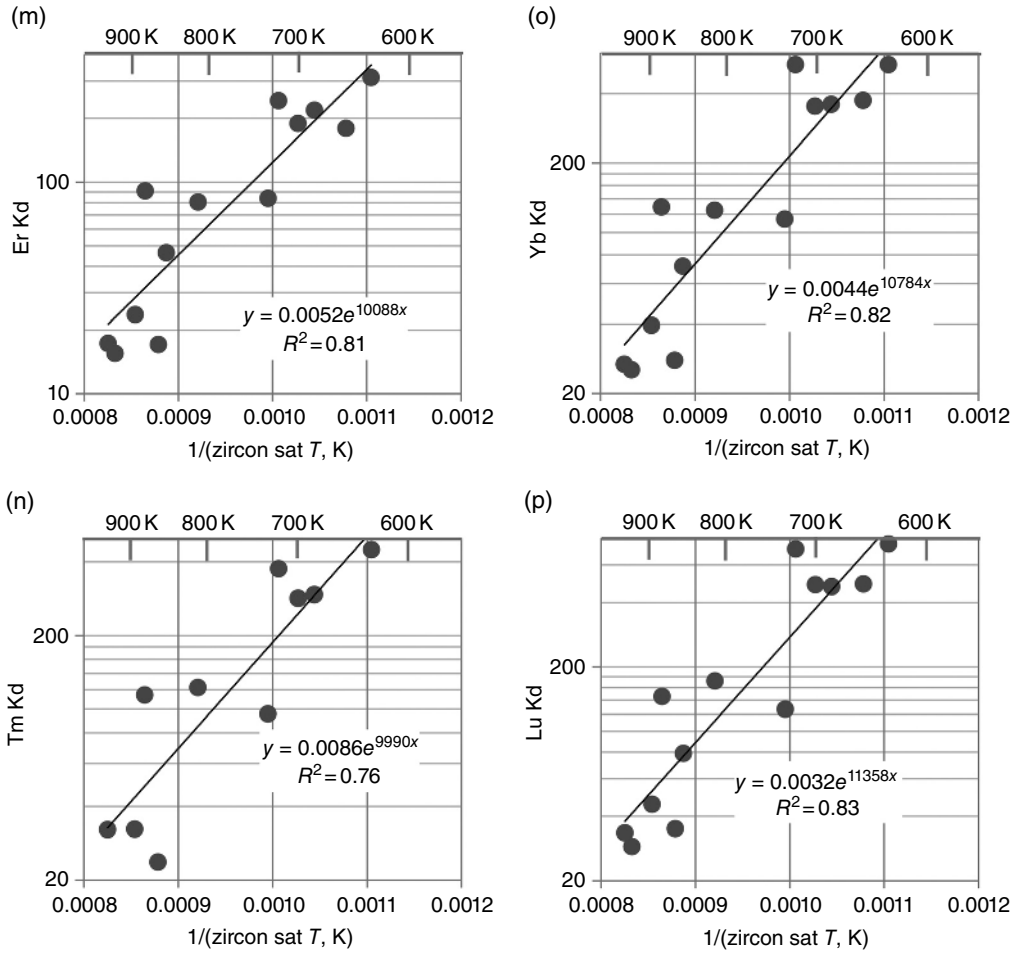

Figure 1.9 (Continued)

experiments were at much higher T (1265°C) than those of *Rubatto and Hermann* [2007], or than those that we estimate for growth of zircons in our study, and lower Kds are thus predicted. Furthermore, the slope of the REE Kd pattern determined by *Burnham and Berry* [2012] is gentler than those for our lower-T zircons, as predicted by our study.

The principal discrepancy between our Kds and those of a majority of previous studies is that our Kds for LREE are lower, in some cases far lower. As we demonstrated in our discussion of lattice strain modeling of REE Kds, even our values for La and probably Nd are too high, a consequence of tiny mineral and/or melt inclusions that are unavoidable by SHRIMP. We note that the LREE results of *Sano et al.* [2002], whose approach was similar to ours (SIMS analysis of zircon rims and glass), matched ours; we suspect that their values were also slightly contaminated by inclusions. Other studies used whole zircons or in situ analyses with larger analytical volumes (LA-ICP-MS) and hence were prone to much larger LREE contamination by inclusions.

1.6.2. Titanium in Zircon as a Guide to Estimation of Kds and Compositions of "Lost" Melts

Regardless of the underlying cause or causes, zircon demonstrates a clear negative Kd-T correlation that can be usefully applied to estimate compositions of melts from which zircon zones crystallized if the temperature of crystallization can be constrained. Unless a zircon crystal contains inclusions that can serve as geothermometers, which may rarely be the case [e.g., *Hopkins et al.*, 2010; *Jennings et al.*, 2011], the temperature constraint must be intrinsic to the zircon. At present, the only promising measurable parameter is Ti concentration [*Watson and Harrison*, 2005; *Ferry and Watson*, 2007].

As discussed in section 1.3, serious concerns have been raised about the Ti-in-zircon thermometer as a reliable way to obtain precise and accurate temperature estimates, especially if there is no other record of the growth environment (e.g., to constrain a_{TiO_2}). Nonetheless, Ti concentration in zircon correlates with temperature of zircon growth; thus, it can provide a valuable qualitative to semi-quantitative indicator of T. Given the enormous variability

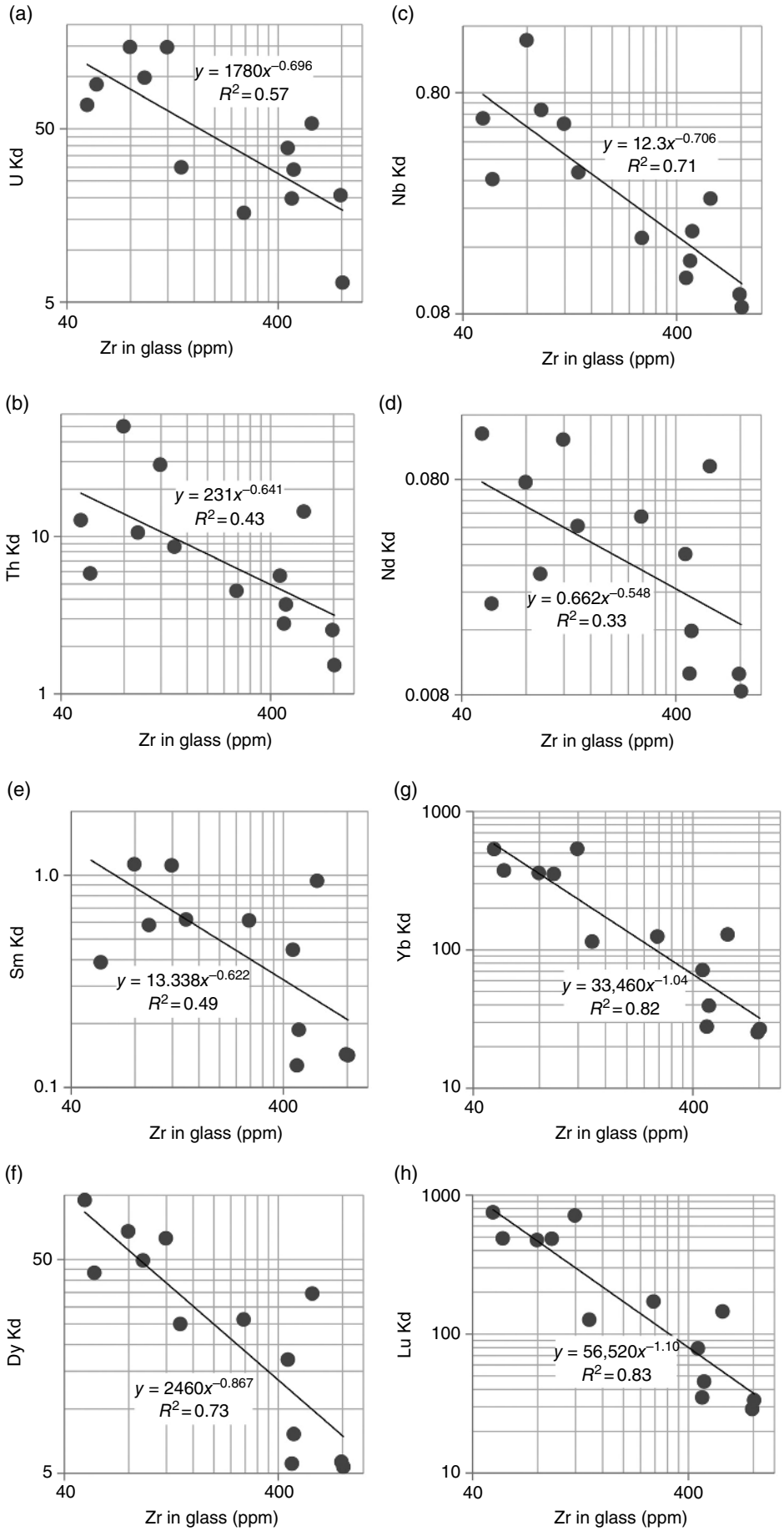

Figure 1.10 $Kds^{zircon/melt}$ versus Zr concentration in melt (glass). (a) U Kd; (b) Th Kd; (c) Nb Kd; (d) Nd Kd; (e) Sm Kd; (f) Dy Kd; (g) Yb Kd; and (h) Lu Kd.

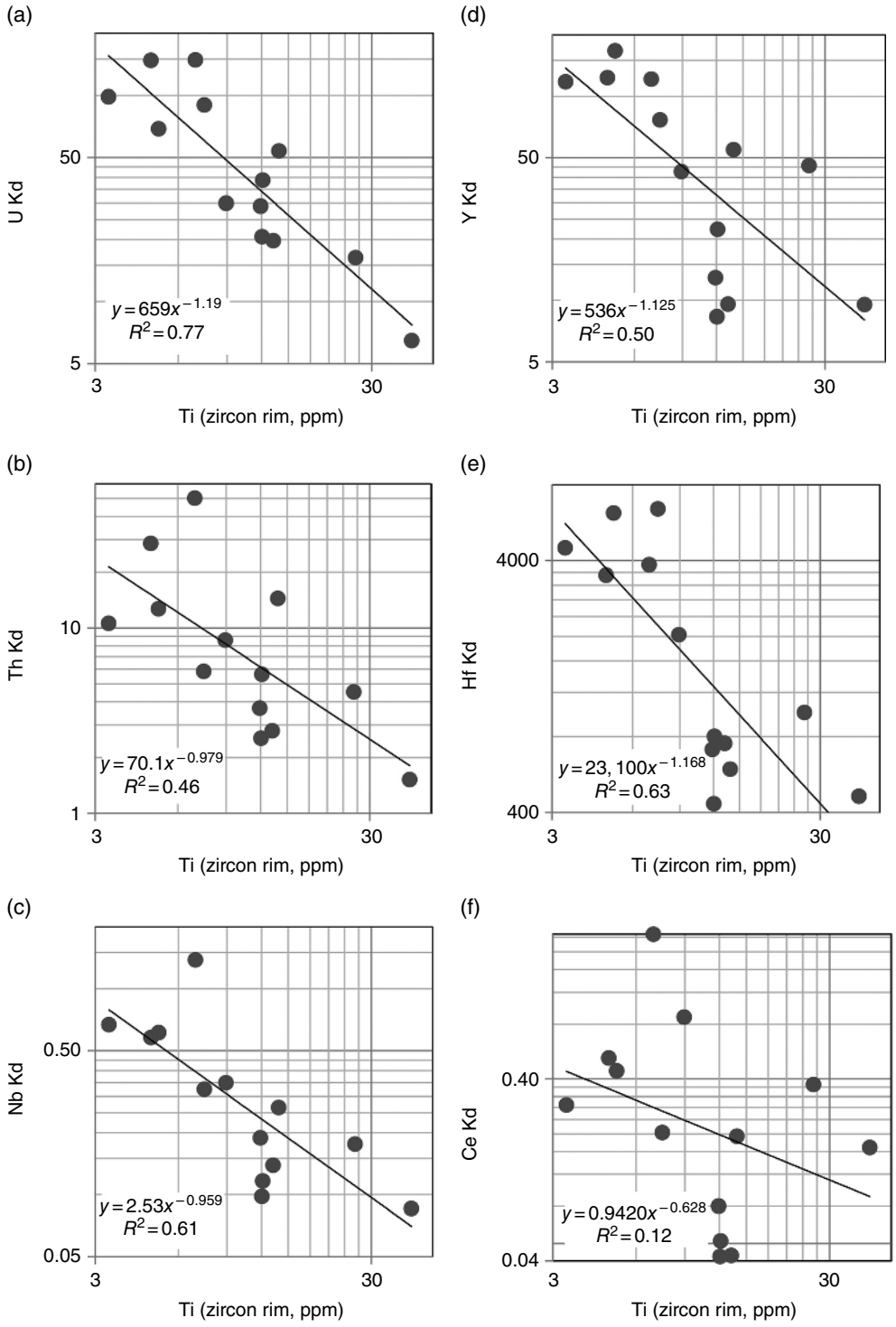

Figure 1.11 $Kds^{zircon/melt}$ versus Ti concentration in zircon rim or surface (ppm) with correlations. (a) U Kd; (b) Th Kd; (c) Nb Kd; (d) Y Kd; (e) Hf Kd; (f) Ce Kd; (g) Nd Kd; (h) Sm Kd; (i) Eu Kd; (j) Gd Kd; (k) Dy Kd; (l) Tb Kd; (m) Ho Kd; (n) Er Kd; (o) Tm Kd; (p) Yb Kd; and (q) Lu Kd.

in zircon Kds, the evident correlation between temperature and Kds (Figs. 1.8 and 1.9), and the absence of any other measurable parameter retained by zircon that has been shown to directly reflect T, we propose that estimates of zircon Kds based on observed Kd-Ti_{zircon} correlations will prove useful in constraining the compositions of the "lost" melts (and by implication magmas) from which detrital zircons and interior zircon zones grew. In Figure 1.11 and Table 1.5, we present the observed relationships. Correlations are, not surprisingly, far from

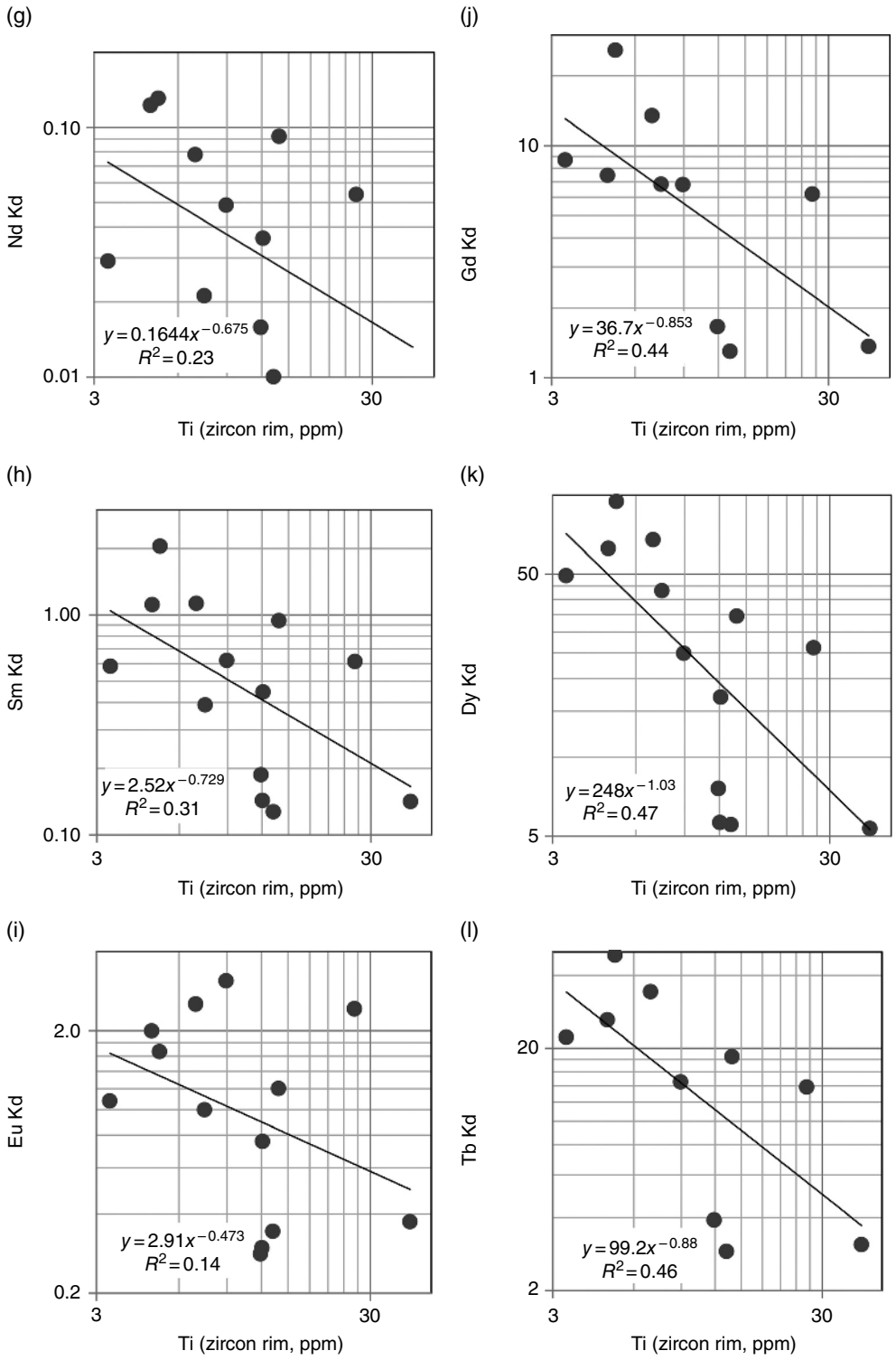

Figure 1.11 (Continued)

perfect, but best fit equations yield uncertainties much smaller than the total range (well under half an order of magnitude uncertainties, compared with well over an order of magnitude ranges for individual elements).

In the following section, we present a case study using Kds estimated in this way to reconstruct melt compositions through time recorded by zircon interiors from MSH.

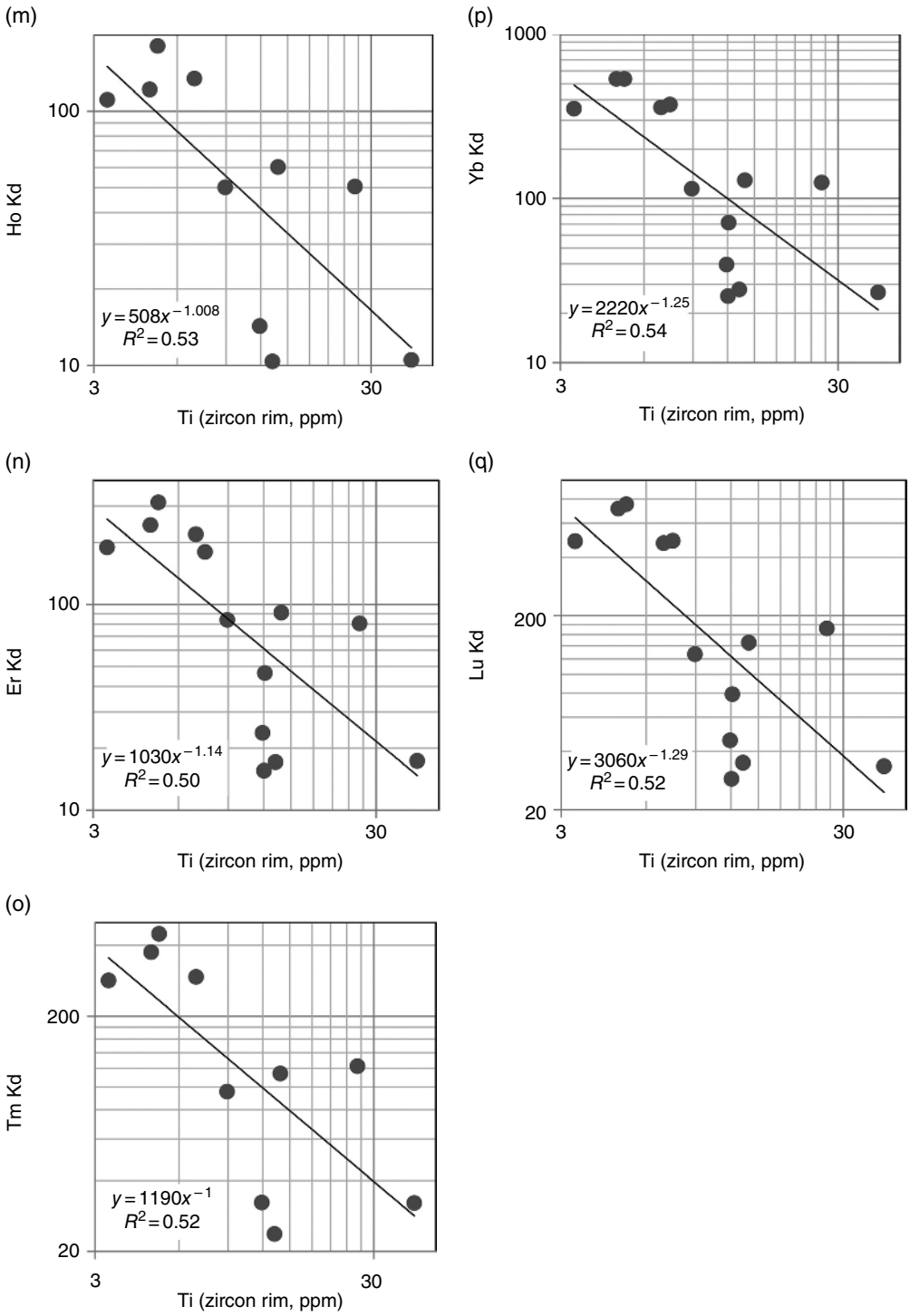

Figure 1.11 (Continued)

1.6.3. Applying New Ti-calibrated Kds: Evaluating the Magmatic History of MSH

MSH has an approximately 300 kyr eruption history [*Clynne et al.*, 2008], with evidence that the earliest activity in the magmatic system began ~500 ka [*Claiborne et al.*, 2010]. Uranium-Series disequilibria in MSH dacites and plagioclase suggest that the bulk of the magma (melt and crystals) that erupts from MSH ascended from genesis in the lower crust to eruption in only a few thousand years, suggesting little time of storage in the crust [*Cooper and Donnelly*, 2008]. Zircons from these same units, however,

Table 1.5 Kd Versus Ti in Zircon (ppm) Correlations

	Best Fit Kd[a]	r^2	Standard Deviation[b]
Th Kd	$70.1*[Ti]^{-0.979}$	0.46	0.30
U Kd	$659*[Ti]^{-1.191}$	0.77	0.19
Nb Kd	$2.53*[Ti]^{-0.959}$	0.61	0.22
Y Kd	$536*[Ti]^{-1.125}$	0.50	0.32
Hf Kd	$23108*[Ti]^{-1.168}$	0.63	0.26
Ce Kd	$0.942*[Ti]^{-0.628}$	0.12	0.48
Nd Kd	$0.164*[Ti]^{-0.675}$	0.23	0.36
Sm Kd	$2.52*[Ti]^{-0.729}$	0.31	0.31
Eu Kd	$2.91*[Ti]^{-0.473}$	0.14	0.33
Gd Kd	$36.7*[Ti]^{-0.853}$	0.44	0.31
Tb Kd	$99.2*[Ti]^{-0.88}$	0.46	0.31
Dy Kd	$248*[Ti]^{-1.03}$	0.47	0.31
Ho Kd	$508*[Ti]^{-1.008}$	0.53	0.31
Er Kd	$1027*[Ti]^{-1.136}$	0.5	0.31
Tm	$1379*[Ti]^{-1.077}$	0.56	0.32
Yb Kd	$2223*[Ti]^{-1.249}$	0.54	0.31
Lu Kd	$3060*[Ti]^{-1.291}$	0.52	0.33

[a] Power law fit; [Ti] = Ti in zircon rim or surface, ppm.
[b] Log units.

$Zr/Hf^{zrc/melt}$ ~1.34+/0.13

(Zr in zircon assumed to be 480,000 ppm; not temperature-sensitive)

record residence for thousands to hundreds of thousands of years in an active plutonic system where some magmas stall, cool significantly, and then are rapidly rejuvenated, mixed, and incorporated into erupting young magmas [*Claiborne et al.*, 2010]. Due to this mixing of stored components, the zircon population of each sample from MSH provides a record of much of the magmatic history of the system and no zircon is entirely cognate to its final host melt. Inferring magmatic compositions directly from zircon composition, the geochemical and geochronological records of these zircons suggest an increase in diversity of magmatic compositions at MSH, ranging to less evolved and higher temperature, at around ~60 ka [*Claiborne et al.*, 2010]. This shift in magmatic character at depth is not evident in erupted materials (other than the zircon record) until ~20 ka, hinting at the power of the extended zircon record to elucidate magmatic processes at depth.

While zircon compositions paired with ages in this way can provide clues to variations in magma compositions through time in the subvolcanic system, the dependence of partitioning on parameters such as temperature and H_2O muddles this record. Applying our new Ti-dependent Kds to the conventionally analyzed trace element compositions of the MSH zircons from these samples, paired with precise U-Th disequilibria ages [*Claiborne et al.*, 2010] should more accurately elucidate the compositional history of the melts that contribute to MSH volcano.

1.6.3.1. Model Melt Results

We calculated model melts by applying our new Ti-calibrated Kd equations to a total of 55 conventional in situ zircon SHRIMP analyses from these three samples, which all have paired zircon composition and age data. Ages are primarily model ages from U-Th disequilibria dating; the oldest ages, which exceed the maximum that can be determined accurately by U-Th, were measured by U-Pb analysis.

Model melt U and Th concentrations are positively correlated, with 90% falling between ~0.5 and 10 ppm, and ~1–35 ppm, respectively (Fig. 1.12), with 90% of Th/U ranging from ~1 to 6. Median concentrations

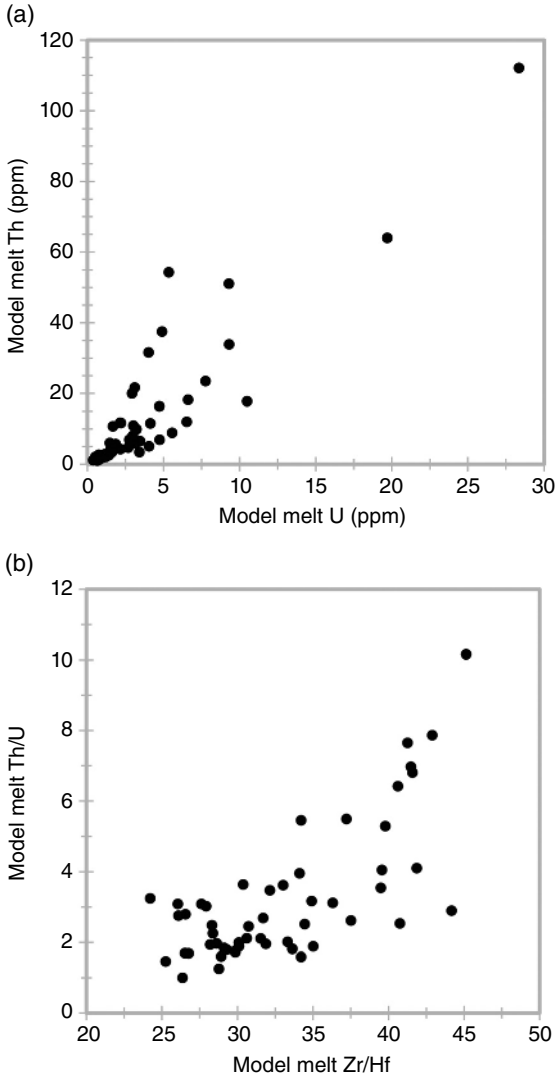

Figure 1.12 Trace element compositions of MSH model melts, based on application of new Ti-dependent Kds to conventional SHRIMP analysis of polished zircon interiors, including cores and rims, from three samples (SHL21Z, SHL26Z, and SHL34Z). (a) Model melt U (ppm) versus model melt Th (ppm) and (b) model melt Zr/Hf versus model melt Th/U.

(U = 3.0 ppm, Th = 6.7 ppm, Th/U = 2.6) are not unlike measured glass compositions from MSH, giving us confidence that the modeled melts are, overall, reliable. Model melts exhibit REE patterns typical of felsic magmas (Fig. 1.13), more enriched in LREE and more depleted in HREE, with variation of a factor of ~2–5 for the most coherent 90% of analyses, depending on the sample. Elements vary systematically, with the exception of Nd, which in a few cases differs greatly from expected values. Europium and Ce vary, but unsurprisingly, as effects of oxidation on these multivalent cations render the Kds less reliable than for the other trivalent REEs.

Model MSH melts are diverse in trace element composition at any given time, but they also reveal patterns of variation through time (Fig. 1.14). Variability is much greater during the past 60–100 kyr, with ranges to much higher Th/U, Zr/Hf, and MREE/HREE.

1.6.3.2. Implications for MSH Magmatic System

The modeled melt compositions support other indications that early magmas were cool and wet and later magmas were more diverse, including higher temperature magmas with lower water contents [*Clynne et al.*, 2008]. The presence of diverse melts at any one time suggests that beneath MSH, discrete pockets of melt are crystallizing zircon as they cool and solidify in isolation from one another. This supports recent studies that suggest similar histories for other magmatic systems, including South Sister, another Cascade Arc volcano [*Stelten and Cooper*, 2012]. Our results also support the conclusion, previously drawn

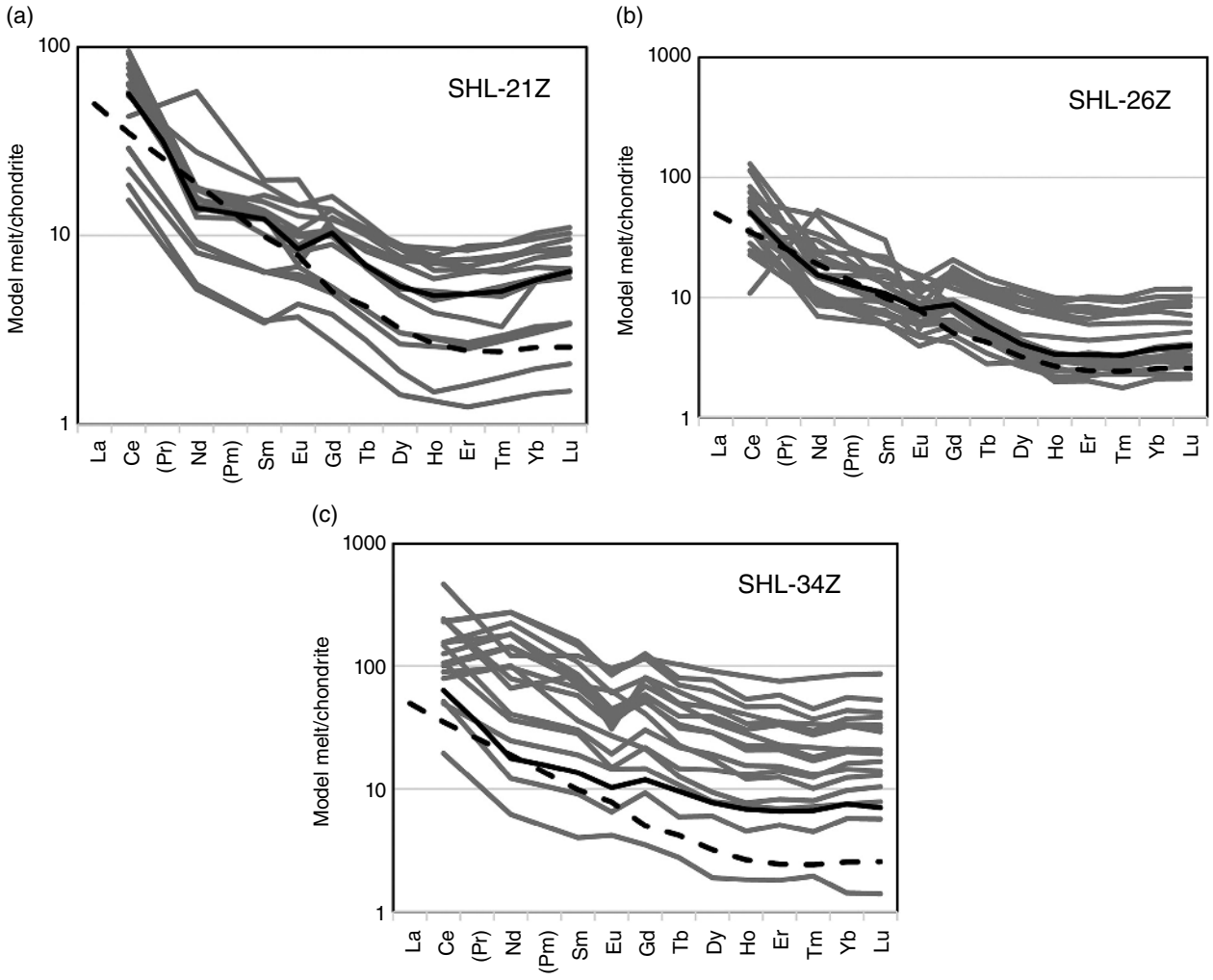

Figure 1.13 REE model melt/chondrite patterns for Mount St. Helens, based on application of Ti-dependent Kds to conventional SHRIMP analysis of polished zircon interiors, including cores and rims. Pr and Pm, shown in parentheses, were not analyzed for any samples, and Tb, Ho, Tm only for some. Missing elements are calculated as midpoints between elements of adjacent atomic number. (a–c) Model melt REE patterns for samples SHL21Z, SHL26Z, and SHL34Z, respectively. The solid black line represents the median model melt composition for each sample. The dashed black line represents the average glass composition of each sample.

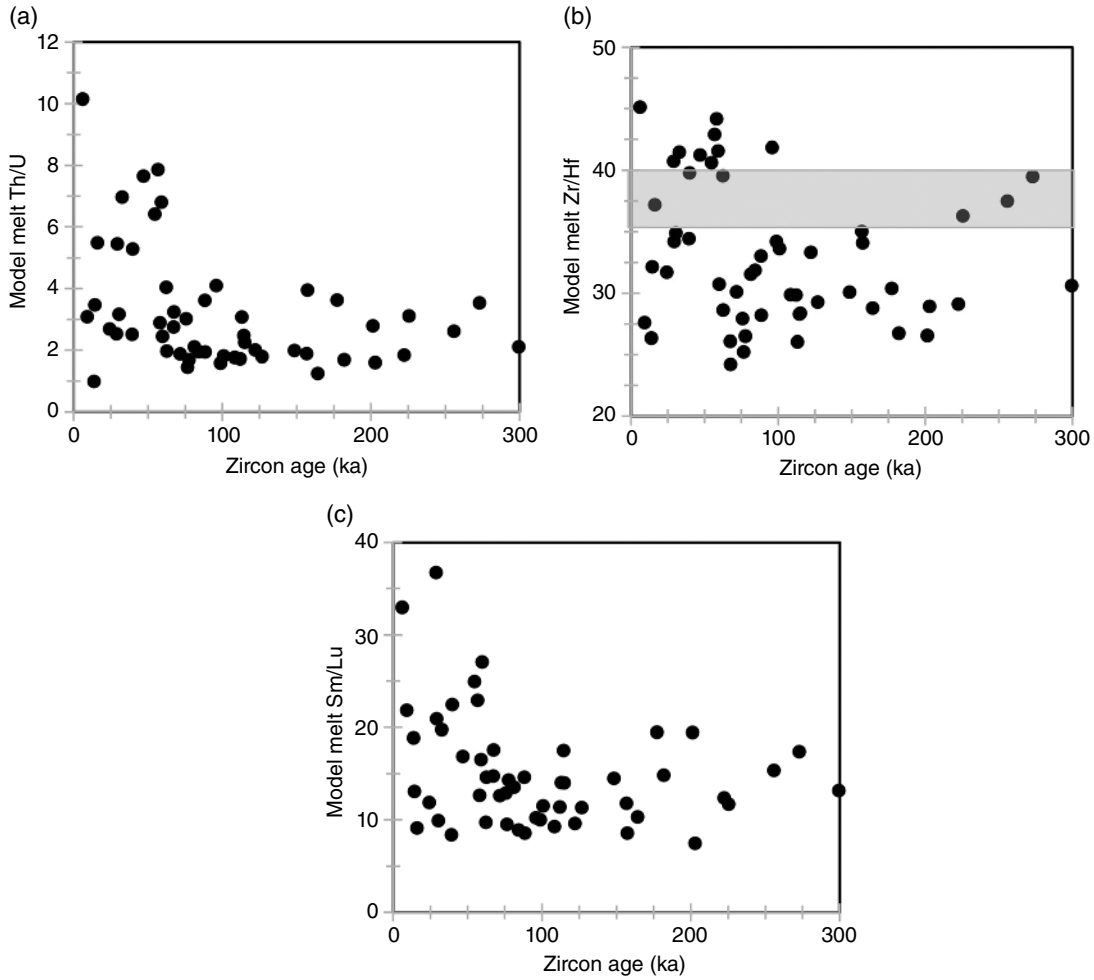

Figure 1.14 Zircon age versus model melt trace element ratios for Mount St. Helens, based on application of new, Ti-dependent Kds to conventional SHRIMP analysis of polished zircon interiors, including cores and rims. Zircon ages from U-Th and U-Pb SHRIMP analyses. (a) Th/U and (b) Zr/Hf. The gray bar represents chondritic Zr/Hf [*Ahrens and Erlank*, 1969; *Hoskin and Schaltegger*, 2003]; (c) Sm/Lu.

from the zircon compositions themselves [*Claiborne et al.*, 2010], that magmas intruding the MSH active plutonic system diversified and were influenced by hotter, drier, less evolved melts ~40–80 kyr before more diverse melts began to erupt. While the variability in zircon composition could be attributed to a variety of factors, modeling melts with our new Ti-dependent Kds strengthen confidence in the conclusion that the melt compositions do change character.

1.7. CONCLUSIONS

1. We present measured zircon/glass Kds for Nb, U, Th, Y, Hf, and 14 REE for 13 samples from diverse tectonomagmatic settings that are robust (except for La and possibly Nd), based upon the following evidence:
   a. The REE, except for La, Ce, Nd, and Eu, fit very well with reasonable lattice strain models.
   b. All Kds are consistent with the most reliable published data.
2. Regarding La, Ce, Nd, and Eu, we suggest the following:
   a. Valid Kds for La and possibly Nd are unattainable by our approach or any other that has been attempted to date, because true concentrations of La are so low that they are difficult to measure, and La in minute inclusions of almost any phase within the analyzed volume overwhelms the contribution from zircon. Our calculated La Kds are as low as any yet proposed, but they are still serious overestimates. Neodymium Kds determined carefully, including ours, may approach true values, but they are nonetheless also likely to be overestimates.
   b. We believe that our individual measured Kds for Ce and Eu are valid, but, because we do not have good

constraints on f_{O_2}, we do not advocate their general use. Combining our REE Kds for trivalent REE with experimental Kd studies that controlled f_{O_2} or studies of natural samples with well-constrained f_{O_2},may provide useful values.

3. We confidently propose Kds for all elements that vary by ~1.5 orders of magnitude over the range of conditions represented by our samples. This verifies the indication from previous work that zircon Kds are highly variable, but our new Kds are much more tightly constrained and vary more consistently from element to element and sample to sample than published values as a whole: that is, ratios of Kds are quite consistent (visible in the parallel patterns). Some potentially important observations in detail about Kd ratios are as follows:
   a. There is a positive correlation between REE Kd ratios and magnitude of Kd (which correlates inversely with *T*, see conclusion (4)): that is, the positive slope of the Kd pattern is steeper for samples with higher Kds (lower *T*).
   b. $Zr/Hf^{zircon/melt}$ is fairly uniform and appears to be independent of Hf Kd or *T*; it is ~1.4.
   c. Kd_{Th}/Kd_{U} shows moderate variation but appears to be independent of measured or estimated parameters; the variation may simply reflect variation in f_{O_2}.
4. Comparison of Kds calculated using analyses of eruption-age surfaces (crystal faces) with adhering glass, which we consider to be the most reliable method, with those determined from conventional analyses of rim zones in polished cross sections, yield results that are similar enough that we consider the latter approach to be acceptable.
5. With the exceptions of La, Ce, Nd, and Eu (for reasons suggested above), all of our measured Kds for individual elements correlate very well with proxies for temperature: Zr and the derived quantity zircon saturation *T*, and Ti in zircon. They do not correlate with compositional parameters for coexisting glasses (A/CNK, SiO_2, M factor of *Watson and Harrison* [1983], FM factor of *Ryerson and Watson* [1987]); this may be in part because glass compositions in our samples did not vary a great deal, but a majority of zircon-saturated melts in nature likewise fall in a relatively restricted range. A majority of the > order of magnitude variation in Kds can be accounted for by the *T* correlation.
6. Correlation of Kds with Ti concentration in zircon (proxy for *T*) permits useful approximate estimation of Kds for any zone in magmatic zircon. We provide best fit equations for Kds as a function of Ti_{zircon} that can be used to estimate the melt compositions of "lost" magmas from which zircon zones grew. It may be especially useful for detrital zircon studies, but is also applicable to tracing evolution of magmatic systems through analysis of zircon interiors.
7. Application of our Ti-correlated Kds to dated interiors of zircons documents a magmatic compositional history at MSH that is consistent with that suggested by previous large-scale studies. This supports the validity of the approach that we propose.

ACKNOWLEDGEMENTS

We thank Desmond Moser for his support as Guest Editor of this volume and Dustin Trail for his careful and helpful review. We benefited from glass analyses performed by Dylan Thomas and Saba Asefa. Our research was supported by NSF grants EAR-0635922 and 1220523.

REFERENCES

Abbey, S. (1983), Studies in "standard samples" of silicate rocks and minerals 1969–1982, *Can. Geol. Survey Pap.*, *83–15*, 114.

Ahrens, L. H., and A. J. Erlank (1969), Hafnium, in *Handbook of Geochemistry*, vol. *sections B-O*, edited by K. H. Wedepohl, pp. 2–5, Springer, Berlin.

Bachmann, O., M. A. Dungan, and F. Bussy (2005), Insights into shallow magmatic processes in large silicic magma bodies: The trace element record in the Fish Canyon magma body, Colorado, *Contrib. Mineral. Petrol.*, *149*, 338–349.

Baker, D. R., A. M. Conte, C. Freda, and L. Ottolini (2002), The effect of halogens on Zr diffusion and zircon dissolution in hydrous metaluminous granitic melts, *Contrib. Mineral. Petrol.*, *142*, 666–678.

Barboni, M., P. Boehnke, A. K. Schmitt, T. M. Harrison, P. Shane, A. S. Bouvier, and L. Baumgartner (2016), Warm storage for arc magmas, *Proc. Natl. Acad. Sci.*, *113*(49), 13959–13964.

Bea, F., M. D. Pereira, and A. Stroh (1994), Mineral/leucosome trace-element partitioning in a peraluminous migmatite (a laser ablation-ICP-MS study), *Chem. Geol.*, *117*, 291–312.

Bell, E. A., T. M. Harrison, I. E. Kohl, and E. D. Young (2014), Eoarchean crustal evolution of the Jack Hills zircon source and loss of Hadean crust, *Geochim. Cosmochim. Acta*, *146*, 27–42.

Blundy, J., and B. Wood (1994), Prediction of crystal-melt partition coefficients from elastic moduli, *Nature*, *372*, 452–454.

Blundy, J., and B. Wood (2003), Partitioning of trace elements between crystals and melts, *Earth Planet. Sci. Lett.*, *210*, 383–397.

Boehnke, P., E. B. Watson, D. Trail, T. M. Harrison, and A. K. Schmitt (2013), Zircon saturation re-revisited, *Chem. Geol.*, *351*, 324–334.

Burnham, A. D., and A. J. Berry (2012), An experimental study of trace element partitioning between zircon and melt as a function of oxygen fugacity, *Geochim. Cosmochim. Acta*, *95*, 196–212.

Carley, T. L., C. F. Miller, J. L. Wooden, I. N. Bindeman, and A. P. Barth (2011), Zircon from historic eruptions in Iceland:

Reconstructing storage and evolution of silicic magmas, *Mineral. Petrol.*, *102*, 135, doi:10.1007/s00710-011-0169-3.

Carley, T. L., C. F. Miller, J. L. Wooden, A. J. Padilla, A. K. Schmitt, R. C. Economos, I. N. Bindeman, and B. T. Jordan (2014), Iceland is not a magmatic analog for the Hadean: Evidence from the zircon record, *Earth Planet. Sci. Lett.*, *405*, 85–97.

Chamberlain, K. J., C. J. N. Wilson, J. L. Wooden, B. L. A. Charlier, and T. R. Ireland (2014), New perspectives on the bishop tuff from zircon textures, ages and trace elements, *J Petrol.*, *55*(2), 395–426.

Claiborne, L. L., C. F. Miller, B. A. Walker, J. L. Wooden, F. K. Mazdab, and F. Bea (2006), Tracking magmatic processes through Zr/Hf ratios in rocks and Hf and Ti zoning in zircons: An example from the Spirit Mountain batholith, Nevada, *Mineral. Mag.*, *70*(5), 517–543.

Claiborne, L. L., C. F. Miller, D. F. Flanagan, M. A. Clynne, and J. L. Wooden (2010), Zircon reveals protracted magma storage and recycling beneath Mount St. Helens, *Geology*, *38*, 1011–1014, doi:10.1130/G31285.1.

Clynne, M. A., A. T. Calvert, E. W. Wolfe, R. C. Evarts, R. J. Fleck, and M. A. Lanphere (2008), The Pleistocene eruptive history of Mount St. Helens, Washington, from 300,000 to 12,000 years before present, in *A Volcano Rekindled: The Renewed Eruption of Mount St. Helens, 2004–2006*, U.S. Geological Survey Professional Paper 1750, edited by D. R. Sherrod et al., pp. 593–627, U.S. Geological Survey, Reston, VA.

Colombini, L. L. (2009), Mid-Miocene rhyolite sequence, Highland Range, NV: Record of magma evolution and eruption from the Searchlight pluton magma chamber, Master's thesis, Vanderbilt University, Nashville, TN.

Colombini, L. L., C. F. Miller, G. A. R. Gualda, J. L. Wooden, and J. S. Miller (2011), Sphene and zircon in the Highland Range volcanic sequence (Miocene, southern Nevada, USA): Elemental partitioning, phase relations, and influence on evolution of silicic magma, *Mineral. Petrol.*, *102*, 29–50.

Compston, W., and R. T. Pidgeon (1986), Jack Hills, evidence of more very old detrital zircons in Western Australia, *Nature*, *321*, 766–769, doi:10.1038/321766a0.

Condie, K. C., M. E. Bickford, R. C. Aster, E. Belousova, and D. W. Scholl (2011), Episodic zircon ages, Hf isotopic composition, and the preservation rate of continental crust, *Geol. Soc. Am. Bull.*, *123*, 951–957.

Cooper, K. M., and C. T. Donnelly (2008), 238U-230Th-226Ra disequilibria in dacite and plagioclase from the 2004–2005 eruption of Mount St. Helens, in *A Volcano Rekindled: The Renewed Eruption of Mount St. Helens, 2004–2006*, U.S. Geological Survey Professional Paper 1750, edited by D. R. Sherrod et al., pp. 827–846, U.S. Geological Survey, Reston, VA.

Ferguson, C. A., W. C. McIntosh, and C. F. Miller (2013), Tectonically dismembered source caldera for the Peach Spring Tuff is a potential three-dimensional strain-marker in the Colorado River extensional corridor, *Geology*, *41*, 3–6, doi:10.1130/G33551.1.

Ferry, J. M., and E. B. Watson (2007), New thermodynamic models and revised calibrations for the Ti-in-zircon and Zr-in-rutile thermometers, *Contrib. Mineral. Petrol.*, *154*, 429–437.

Froude, D. O., T. R. Ireland, P. D. Kinny, I. S. Williams, W. Compston, I. T. Williams, and J. S. Myers (1983), Ion microprobe identification of 4,100–4,200 Myr-old terrestrial zircons, *Nature*, *304*, 616–618.

Fujimaki, H. (1986), Partition coefficients of Hf, Zr, and REE between zircon, apatite, and liquid, *Contrib. Mineral. Petrol.*, *94*, 42–45.

Gervasoni, F., S. Klemme, E. R. V. Rocha Jr., and J. Berndt (2016), Zircon saturation in silicate melts: A new and improved model for aluminous and alkaline melts, *Contrib. Mineral. Petrol.*, *171*, 21.

Ghiorso, M. S., and G. A. R. Gualda (2013), A method for estimating the activity of titania in magmatic liquids from the compositions of coexisting rhombohedral and cubic iron-titanium oxides, *Contrib. Mineral. Petrol.*, *165*, 73–81.

Govindaraju, K. (1994), 1994 compilation of working values and sample description for 383 geostandards, *Geostand. Geoanal. Res.*, *18*, 1–158.

Griffin, W. L., W. J. Powell, N. J. Pearson, and S. Y. O'reilly (2008), GLITTER: Data reduction software for laser ablation ICP-MS, in *Laser Ablation-ICP-MS in the earth sciences*, Mineralogical association of Canada short course series, vol. 40, edited by P. Sylvester, pp. 204–207, Mineralogical Association of Canada, Ottawa.

Grimes, C. B., J. L. Wooden, M. J. Cheadle, and B. E. John (2015), "Fingerprinting" tectono-magmatic provenance using trace elements in igneous zircon, *Contrib. Mineral. Petrol.*, *170*, 46, doi:10.1007/s00410-015-1199-3.

Gualda, G. A. R., A. S. Pamukcu, L. L. Claiborne, and M. L. Rivers (2010), Quantitative 3D petrography using x-ray tomography. 3: Documenting accessory phases with differential absorption tomography, *Geosphere*, *6*, 782–792.

Hanchar, J. M., and W. van Westrenen (2007), Rare earth element behavior in zircon-melt systems, *Elements*, *3*, 37–42.

Hanchar, J. M., and E. B. Watson (2003), Zircon saturation thermometry, *Rev. Mineral. Geochem.*, *53*, 89–112.

Hanchar, J. M., R. J. Finch, P. W. Hoskin, E. B. Watson, D. J. Cherniak, and A. N. Mariano (2001), Rare earth elements in synthetic zircon: Part 1. Synthesis, and rare earth element and phosphorus doping, *Am. Mineral.*, *86*, 667–680.

Harrison, T. M. (2009), The Hadean crust: Evidence from > 4 Ga zircons, *Annu. Rev. Earth Planet. Sci.*, *37*, 479–505.

Harrison, T. M., and E. B. Watson (1984), The behavior of apatite during crustal anatexis: Equilibrium and kinetic considerations, *Geochim. Cosmochim. Acta*, *48*, 1467–1477.

Hawkesworth, C. J., P. A. Cawood, and B. Dhuime (2016), Tectonics and crustal evolution, *GSA Today*, 4–11.

Hofmann, A. E., J. W. Valley, E. B. Watson, A. J. Cavosie, and J. M. Eiler (2009), Sub-micron scale distributions of trace elements in zircon, *Contrib. Mineral. Petrol.*, *158*, 317–335.

Hofmann, A. E., M. B. Baker, and J. M. Eiler (2013), An experimental study of Ti and Zr partitioning among zircon, rutile, and granitic melt, *Contrib. Mineral. Petrol.*, *166*, 235–253.

Hofmann, A. E., M. B. Baker, and J. M. Eiler (2014), Sub-micron-scale trace-element distributions in natural zircons of known provenance: Implications for Ti-in-zircon thermometry, *Contrib. Mineral. Petrol.*, *168*, 1057.

Hopkins, M. D., T. M. Harrison, and C. E. Manning (2010), Constraints on Hadean geodynamics from mineral inclusions in > 4Ga zircons, *Earth Planet. Sci. Lett.*, *298*, 367–376.

Hoskin, P. W., and U. Schaltegger (2003), The composition of zircon and igneous and metamorphic petrogenesis, *Rev. Mineral. Geochem.*, *53*, 27–62.

Jakobsson, S. P., K. Jónasson, and I. A. Sigurdsson (2008), The three igneous rock series of Iceland, *Jökull*, *58*, 117–138.

Jennings, E. S., H. R. Marschall, C. J. Hawkesworth, and C. D. Storey (2011), Characterization of magma from inclusions in zircon: Apatite and biotite work well, feldspar less so, *Geology*, *39*, 863–866.

Jochum, K. P., U. Weis, B. Stoll, D. Kuzmin, Q. Yang, I. Raczek, D. E. Jacob, A. Stracke, K. Birbaum, D. A. Frick, and D. Günther (2011), Determination of reference values for NIST SRM 610–617 glasses following ISO guidelines, *Geostand. Geoanal. Res.*, *35*, 397–429.

Jónasson, K., P. M. Holm, and A. K. Pedersen (1992), Petrogenesis of silicic rocks from the Króksfjördur central volcano, NW Iceland, *J. Petrol.*, *33*, 1345–1369.

Kemp, A. I. S., C. J. Hawkesworth, B. A. Paterson, G. L. Foster, P. D. Kinny, M. J. Whitehouse, and R. Maas (2006), Exploring the plutonic–volcanic link: A zircon U–Pb, Lu–Hf and O isotope study of paired volcanic and granitic units from southeastern Australia, *Trans. R. Soc. Edinb. Earth Sci.*, *97*, 337–355.

Kemp, A. I. S., C. J. Hawkesworth, G. L. Foster, B. A. Paterson, J. D. Woodhead, J. M. Hergt, C. M. Gray, and M. J. Whitehouse (2007), Magmatic and crustal differentiation history of granitic rocks from Hf-O isotopes in zircon, *Science*, *315*, 980–983.

Kurosawa, M., S. E. Jackson, and S. Sueno (2002), Trace element analysis of NIST SRM 614 and 616 glass reference materials by laser ablation microprobe-inductively coupled plasma-mass spectrometry, *Geostand. Newsl.*, *26*, 75–84.

Luo, Y., and J. C. Ayers (2009), Experimental measurements of zircon/melt trace-element partition coefficients, *Geochim. Cosmochim. Acta*, *73*, 3656–3679.

Maas, R., P. D. Kinny, I. S. Williams, D. O. Froude, and W. Compston (1992), The Earth's oldest known crust: A geochronological and geochemical study of 3900–4200 Ma old detrital zircons from Mt. Narryer and Jack Hills, Western Australia, *Geochim. Cosmochim. Acta*, *56*, 1281–1300.

Mahood, G., and W. Hildreth (1983), Large partition coefficients for trace elements in high-silica rhyolites, *Geochimica and Cosmochimica Acta*, *47*, 11–30.

McDowell, S. M., C. F. Miller, R. Mundil, C. A. Ferguson, and J. W. Wooden (2014), Zircon evidence for a ~200 k.y. supereruption-related thermal flare-up in the Miocene southern Black Mountains, western Arizona, USA, *Contrib. Mineral. Petrol.*, *168*, 1031.

Miller, C. F., S. M. McDowell, and R. W. Mapes (2003), Hot and cold granites? Implications of zircon saturation temperatures and preservation of inheritance, *Geology*, *31*, 529–532.

Mysen, B.O., D. Virgo, and F.A. Siefert, (1985), Relationships between properties and structure of aluminosilicate melts, *A. Mineral.*, *70*, 88–105.

Nagasawa, H. (1970), Rare Earth concentrations in zircons and apatites and their host dacites and granites, *Earth Planet. Sci. Lett.*, *9*, 359–364.

Nardi, L. V. S., M. L. L. Formoso, I. F. Müller, E. Fontana, K. Jarvis, and C. Lamarão (2013), Zircon/rock partition coefficients of REEs, Y, Th, U, Nb, and Ta in granitic rocks: Uses for provenance and mineral exploration purposes, *Chem. Geol.*, *225*, 1–7.

Onuma, N., H. Higuchi, H. Wakita, and H. Nagasawa (1968), Trace element partition between two pyroxenes and the host lava, *Earth Planet. Sci. Lett.*, *5*, 47–51.

Padilla, A. J., and G. A. Gualda (2016), Crystal-melt elemental partitioning in silicic magmatic systems: An example from the Peach Spring Tuff high-silica rhyolite, Southwest USA, *Chem. Geol.*, *440*, 326–344.

Pamukcu, A. S., T. L. Carley, G. A. R. Gualda, C. F. Miller, and C. A. Ferguson (2013), The evolution of the Peach Spring giant magma body: Evidence from accessory mineral textures and compositions, bulk pumice and glass geochemistry, and rhyolite-MELTS modeling, *J. Petrol.*, *54*, 1109–1148.

Pamukcu, A. S., G. A. R. Gualda, M. S. Ghiorso, C. F. Miller, and R. G. McCracken (2015), Phase-equilibrium geobarometers for silicic rocks based on rhyolite-MELTS. Part 3: Application to the Peach Spring Tuff (Arizona-California-Nevada, USA), *Contrib. Mineral. Petrol.*, *169*, 33.

Pearce, N. J. G., W. T. Perkins, J. A. Westgate, M. P. Gorton, S. E. Jackson, C. R. Neal, and S. P. Chenery (1997), A compilation of new and published major and trace element data for NIST SRM 610 and NIST SRM 612 glass reference materials, *Geostand. Newsl.*, *21*, 115–144.

Pedersen, A. K., and N. Hald (1982), A cummingtonite-porphyritic dacite with amphibole-rich xenoliths from the Tertiary central volcano at Kroksfjördur, NW Iceland, *Lithos*, *15*, 137–159.

Reid, M. R., J. A. Vazquez, and A. K. Schmitt (2011), Zircon-scale insights into the history of a Supervolcano, Bishop Tuff, Long Valley, California, with implications for the Ti-in-zircon geothermometer, *Contrib. Mineral. Petrol.*, *161*, 293–311.

Roelandts, I., and E. S. Gladney (1998), Consensus values for NIST biological and environmental standard reference materials, *Fresenius J. Anal. Chem.*, *360*, 327–338.

Rubatto, D., and J. Hermann (2007), Experimental zircon/melt and zircon/garnet trace element partitioning and implications for the geochronology of crustal rocks, *Chem. Geol.*, *241*, 38–61.

Ryerson, F. J., and E. B. Watson (1987), Rutile saturation in magmas: Implications for Ti-Nb-Ta depletion in island-arc basalts, *Earth Planet. Sci. Lett.*, *86*, 225–239.

Sano, Y., K. Terada, and T. Fukuoka (2002), High mass resolution ion microprobe analysis of rare earth elements in silicate glass, apatite and zircon: Lack of matrix dependency, *Chem. Geol.*, *184*, 217–230.

Schmitt, A. K., D. F. Stockli, J. M. Lindsay, R. Robertson, O. M. Lovera, and R. Kislitsyn (2010), Episodic growth and homogenization of plutonic roots in arc volcanoes from combined U–Th and (U–Th)/He zircon dating, *Earth Planet. Sci. Lett.*, *295*, 91–103.

Stelten, M. E., and K. M. Cooper (2012), Constraints on the nature of the subvolcanic reservoir at South Sister volcano,

Oregon from U-series dating combined with sub-crystal trace-element analysis of plagioclase and zircon, *Earth Planet. Sci. Lett.*, *313*, 1–11.

Taylor, R. J. M., S. L. Harley, R. W. Hinton, S. Elphick, C. Clark, and N. M. Kelly (2015), Experimental determination of REE partition coefficients between zircon, garnet and melt: A key to understanding high-T crustal processes, *J. Metamorph. Geol.*, *33*, 231–248.

Thomas, J. B., R. J. Bodnar, N. Shimizu, and A. K. Sinha (2002), Determination of zircon/melt trace element partition coefficients from SIMS analysis of melt inclusions in zircon, *Geochim. Cosmochim. Acta*, *66*, 2887–2901.

Trail, D., J. B. Thomas, and E. B. Watson (2011), The incorporation of hydroxyl into zircon, *Am. Mineral.*, *96*(1), 60–67.

Trail, D., E. B. Watson, and N. Tailby (2012), Ce and Eu anomalies in zircon as proxies for the oxidation state of magmas, *Geochim. Cosmochim. Acta*, *97*, 70–87.

Trail, D., D. J. Cherniak, E. B. Watson, T. M. Harrison, B. P. Weiss, and I. Szumila (2016), Li zoning in zircon as a potential geospeedometer and peak temperature indicator, *Contrib. Mineral. Petrol.*, *171*(3), 1–15.

Valley, J. W., J. S. Lackey, A. J. Cavosie, C. C. Clechenko, M. J. Spicuzza, M. A. S. Basei, I. N. Bindeman, V. P. Ferreira, A. N. Sial, E. M. King, and W. H. Peck (2005), 4.4 billion years of crustal maturation: Oxygen isotope ratios of magmatic zircon, *Contrib. Mineral. Petrol.*, *150*, 561–580.

Watson, E. B. (1976), Two-liquid partition coefficients: Experimental data and geochemical implications, *Contrib. Mineral. Petrol.*, *56*(1), 119–134.

Watson, E. B. (1980), Some experimentally determined zircon/liquid partition coefficients for the rare earth elements, *Geochim. Cosmochim. Acta*, *44*(6), 895–897.

Watson, E. B. (1996), Dissolution, growth and survival of zircons during crustal fusion: Kinetic principles, geological models and implications for isotopic inheritance, *Trans. R. Soc. Edinb. Earth Sci.*, *87*, 43–56.

Watson, E. B., and T. M. Harrison (1983), Zircon saturation revisited: Temperature and composition effects in a variety of crustal magma types, *Earth Planet. Sci. Lett.*, *64*, 295–304.

Watson, E. B., and T. M. Harrison (2005), Zircon thermometer reveals minimum melting conditions on earliest Earth, *Science*, *308*, 841–844.

Willbold, M., E. Hegner, A. Stracke, and A. Rocholl (2009), Continental geochemical signatures in dacites from Iceland and implications for models of early Archaean crust formation, *Earth Planet. Sci. Lett.*, *279*, 44–52.

Wood, B., and J. Blundy (2002), The effect of H2O on crystal-melt partitioning of trace elements, *Geochim. Cosmochim. Acta*, *66*(20), 3647–3656.

Yang, W., Y. Lin, J. Hao, J. Zhang, S. Hu, and H. Ni (2016), Phosphorus-controlled trace element distribution in zircon revealed by NanoSIMS, *Contrib. Mineral. Petrol.*, *171*, 28.